Taylor & Francis
Taylor & Francis Group

Australian Journal of Earth Sciences

An International Geoscience Journal of the Geological Society of Australia

ISSN: (Print) (Online) Journal homepage: https://www.tandfonline.com/loi/taje20

The critical role of deformation-assisted melt migration in the formation of oceanic core complexes

R. L. Gardner, N. R. Daczko & S. Piazolo

To cite this article: R. L. Gardner, N. R. Daczko & S. Piazolo (09 Oct 2023): The critical role of deformation-assisted melt migration in the formation of oceanic core complexes, Australian Journal of Earth Sciences, DOI: 10.1080/08120099.2023.2259451

To link to this article: https://doi.org/10.1080/08120099.2023.2259451

© 2023 The Author(s). Published by Informa UK Limited, trading as Taylor & Francis Group.

Published online: 09 Oct 2023.

Submit your article to this journal

View related articles

View Crossmark data

Full Terms & Conditions of access and use can be found at
https://www.tandfonline.com/action/journalInformation?journalCode=taje20

AUSTRALIAN JOURNAL OF EARTH SCIENCES
https://doi.org/10.1080/08120099.2023.2259451

OPEN ACCESS Check for updates

The critical role of deformation-assisted melt migration in the formation of oceanic core complexes

R. L. Gardner[a], N. R. Daczko[a] and S. Piazolo[b]

[a]Australian Research Council Centre of Excellence for Core to Crust Fluid Systems/GEMOC, School of Natural Sciences, Macquarie University, Sydney, NSW, Australia; [b]School of Earth and Environment, University of Leeds, Leeds, UK

ABSTRACT

Oceanic core complexes provide an accessible window into deep processes occurring at slow and ultra-slow-spreading mid-ocean ridges. We analyse samples from IODP ocean drilling of core complexes at the Atlantis Bank, Atlantis Massif, and near the Kane Transform at the South West Indian and Mid-Atlantic ridges. We correlate secondary minerals, including oxides, with sites of melt migration. We interpret changes to mineral assemblage and microchemistry, reaction textures and melt-pseudomorph microstructures as fingerprints of open-system melt-mediated processes. This micro-scale information is combined with a macro-scale review of legacy mineral chemistry data to show that melt-fluxed rocks share remarkably similar characteristics across the three core complexes investigated. These are rich in oxides and have olivine, orthopyroxene and clinopyroxene grains that are chemically distinct from oxide-poor gabbros. We propose that oceanic crust fluxed with external melt can be recognised by the following key features: (1) high modes of secondary minerals, such as oxides and olivine, (2) microstructural evidence for the former presence of melt, and (3) mineral chemistry differences between primary and secondary olivine, orthopyroxene, clinopyroxene and plagioclase. Importantly, olivine has previously only been reported as primary, that is, having crystallised from magma. However, our results show that gabbros with secondary olivine are reliable indictors of melt–rock interaction during deformation-assisted diffuse melt migration through the gabbroic oceanic crust. Finally, we propose a new model for the formation of oceanic core complexes where deformation-assisted melt migration plays a critical role in strain localisation, exhumation and evolution of the core complex.

KEY POINTS

1. Secondary mineral microstructures indicate the former presence of melt.
2. Olivine, plagioclase and pyroxene chemistry fingerprint melt-fluxed oceanic crust.
3. Evidence of multiple fluxes of external melt associated with strain localisation.
4. High oxide mode and secondary minerals are fingerprints of melt-fluxed zones in oceanic core complexes.

ARTICLE HISTORY
Received 4 July 2023
Accepted 10 September 2023

KEYWORDS
scientific ocean drilling; oceanic core complex; melt–rock interaction; melt-present deformation; strain localisation; Mid-Atlantic Ridge; South West Indian Ridge

Introduction

Oceanic core complexes occur in spatial clusters along slow- and ultra-slow-spreading ridges, where deep crustal rocks are exhumed (Whitney *et al.*, 2013). As such, these complexes reflect regions of moderate magma supply and provide an accessible window into the deep Earth processes of these slow-spreading ridges (Ligi *et al.*, 2022). There is consensus that formation of an oceanic core complex requires a long-lived detachment where strain is highly localised allowing uplift of the complex (Ligi *et al.*, 2022; Whitney *et al.*, 2013). Yet the initiation and development of the detachment are still widely debated (*e.g.* Ligi *et al.*, 2022), even to the point of whether the detachment is initiated in the ductile lower crust and propagates to the upper brittle crust or *vice versa*. Numerical models use a triggering mechanism to initiate the detachment. For example, this can be pre-existing faults in the upper crust (*e.g.* Whitney *et al.*, 2013), density anomalies in the lower crust (*e.g.* Brun *et al.*, 2018) or a strong–weak material discontinuity on the brittle–ductile transition (*e.g.* Wijns *et al.*, 2005).

Suggested triggers of strain localisation on the detachment currently include: (i) infiltration of seawater causing

CONTACT R. L. Gardner robyn.gardner@mq.edu.au Australian Research Council Centre of Excellence for Core to Crust Fluid Systems/GEMOC, School of Natural Sciences, Macquarie University, Sydney, NSW 2109, Australia
Editorial handling: Anita Andrew

© 2023 The Author(s). Published by Informa UK Limited, trading as Taylor & Francis Group.
This is an Open Access article distributed under the terms of the Creative Commons Attribution-NonCommercial-NoDerivatives License (http://creativecommons.org/licenses/by-nc-nd/4.0/), which permits non-commercial re-use, distribution, and reproduction in any medium, provided the original work is properly cited, and is not altered, transformed, or built upon in any way. The terms on which this article has been published allow the posting of the Accepted Manuscript in a repository by the author(s) or with their consent.

exothermic reaction softening with the formation of serpentine and talc (*e.g.* Ildefonse *et al.*, 2007; MacLeod *et al.*, 2009); (ii) grainsize reduction (*e.g.* Harigane *et al.*, 2008); (iii) phase mixing with a switch of deformation mechanism from dislocation creep to diffusion creep (*e.g.* Casini *et al.*, 2021); (iv) weak phases forming shear zones (*e.g.* Agar & Lloyd, 1997); (v) brittle micro-fractures (*e.g.* Miranda & John, 2010; Taufner *et al.*, 2021); and (vi) the physical presence of melt, which causes reaction softening and grainsize reduction along with enhancing melt-assisted grain boundary sliding (*e.g.* Gardner *et al.*, 2020).

Recent work increasingly recognises melt–rock interaction as an important process at oceanic core complexes (*e.g.* Ferrando *et al.*, 2018; Gardner *et al.*, 2020; Ghatak *et al.*, 2022; Lissenberg & MacLeod, 2016; Zhang *et al.*, 2020, 2021). Possible melts that could be involved in melt–rock interactions at mid-ocean ridges include: (1) gabbroic melt formed by partial melting of the mantle during decompression, (2) fractionated gabbroic melt, that is, an intercumulus melt expelled from a compacting crystal mush, (3) melt from partial melting of the oceanic crust (*e.g.* liquids to produce plagio-granites), and (4) any of the above melts modified by melt–rock interaction during migration through the oceanic crust. While melt (1) is thought to be very common and relatively uniform in composition, melts (2) to (4) are volumetrically small and are highly variable in composition.

The rocks exhumed in oceanic core complexes are heterogeneous and include oxide-poor and oxide-rich gabbroic rocks (gabbro, olivine gabbro, norite, gabbronorite and troctolite) (Figure 1d; *e.g.* Blackman, 2006; Cannat *et al.*, 1995; Dick *et al.*, 1999b). While traditionally attributed to closed system magmatic fractionation (melt 2 above), this diversity can also be formed by open-system metasomatism during melt migration and melt–rock interaction (melt 4 above). Both processes form rocks that may display microstructures indicative of the former presence of melt. However, a closed system produces gabbroic rocks with igneous microstructures, whereas the open system forms rocks that may show reaction textures forming secondary high-temperature minerals and mineral/whole-rock chemical zoning (*e.g.* Basch *et al.*, 2022; Dick *et al.*, 2002; Gao *et al.*, 2007; Lissenberg & MacLeod, 2016) depending on the level of equilibration with the interacting melt.

To explore the problem of easily recognising sites of former melt–rock interaction in the oceanic crust, we begin by investigating one of the most extensively sampled oceanic core complexes at Atlantis Bank on the ultra-slow-spreading South West Indian Ridge (Figure 1a). We then extend this analysis with samples from the oceanic core complexes exposed at Atlantis Massif and near the Kane Transform (MARK area) on the slow-spreading Mid-Atlantic Ridge.

This work proposes a simple approach, utilising legacy chemical data, to highlight deformation-assisted migration of a lower temperature oxide-saturated melt in shear zones (Gardner *et al.*, 2020; Ghatak *et al.*, 2022; Zhang *et al.*, 2020). We confirm this simple approach's utility using (1) a detailed microstructural study of two relatively oxide-poor samples from the oxide-rich units III and IV from Atlantis Bank core 735B, (2) new microstructural evaluation of thin-sections from oceanic core complexes at the Atlantis Massif and in the MARK area on the Mid-Atlantic Ridge (Figure 1a), and (3) analysis of legacy micro-chemical data from the three core complexes.

We find that mineral chemistry of rocks associated with oceanic core complexes can be reliably used to identify gabbroic rocks that have experienced significant melt–rock interaction with an oxide-saturated external melt migrating through an active shear zone. The remarkable similarity of geochemical patterns at different oceanic core complexes strongly argues for a common process resulting in the observed heterogeneity of exposed gabbroic rocks. Finally, we present a new model for the development of an oceanic core complex where deformation-assisted melt migration plays a critical role in strain localisation, evolution and exhumation of the oceanic core complex.

Geological background

Atlantis Bank (South West Indian Ridge)

The Atlantis Bank oceanic core complex, on the South West Indian Ridge (SWIR, Figure 1a), now lies ~97 km south of the active ridge, adjacent to the Atlantis II transform valley. The core complex is approximately 30 km long and 12 km wide, and is ~720 m below the sea surface. The longest drilled core at any oceanic core complex is the 735B core (32°43.392′S, 57°15.960′E) at Atlantis Bank (Figure 1b). It was drilled to 1508 m below seafloor (mbsf) on IODP expeditions 118 and 176. The following summary is based on information in Dick *et al.* (1999a, 1999b) unless otherwise specified. The 735B core comprises olivine gabbro (69.9 vol%), gabbro (14.9 vol%), gabbronorite and orthopyroxene-bearing gabbro (5.6 vol%), oxide gabbro (4.5 vol%), oxide gabbronorite and orthopyroxene-bearing oxide gabbro (2.7 vol%), troctolitic gabbro and troctolite (1.9 vol%) and clinopyroxenite (0.04 vol%). These rock types and mineral assemblages were used by the shipboard team to divide the core into 12 rock units (I to XII; Figure 1b). These diverse rock types are cross-cut by microgabbros (2.4 vol%) and felsic veins (0.5 vol%) of leucodiorite, diorite, trondhjemite, tonalite and granite, representing variable fractionation of mid-ocean ridge basalt (Dick *et al.*, 2002; MacLeod *et al.*, 2017), ranging to highly evolved felsic veins (Nguyen *et al.*, 2018; Wolff *et al.*, 2013).

The shipboard party defined the foliation intensity (Figure 1b) by observation: 0, undeformed; to 5, ultramylonite. Approximately 77% of the core lacks a foliation, while 7.1% is strongly foliated or mylonitic at the core scale. Units III and IV are dominated by oxide-rich rocks, and most oxide-rich rocks are strongly correlated with an increase in foliation intensity particularly in the top half of

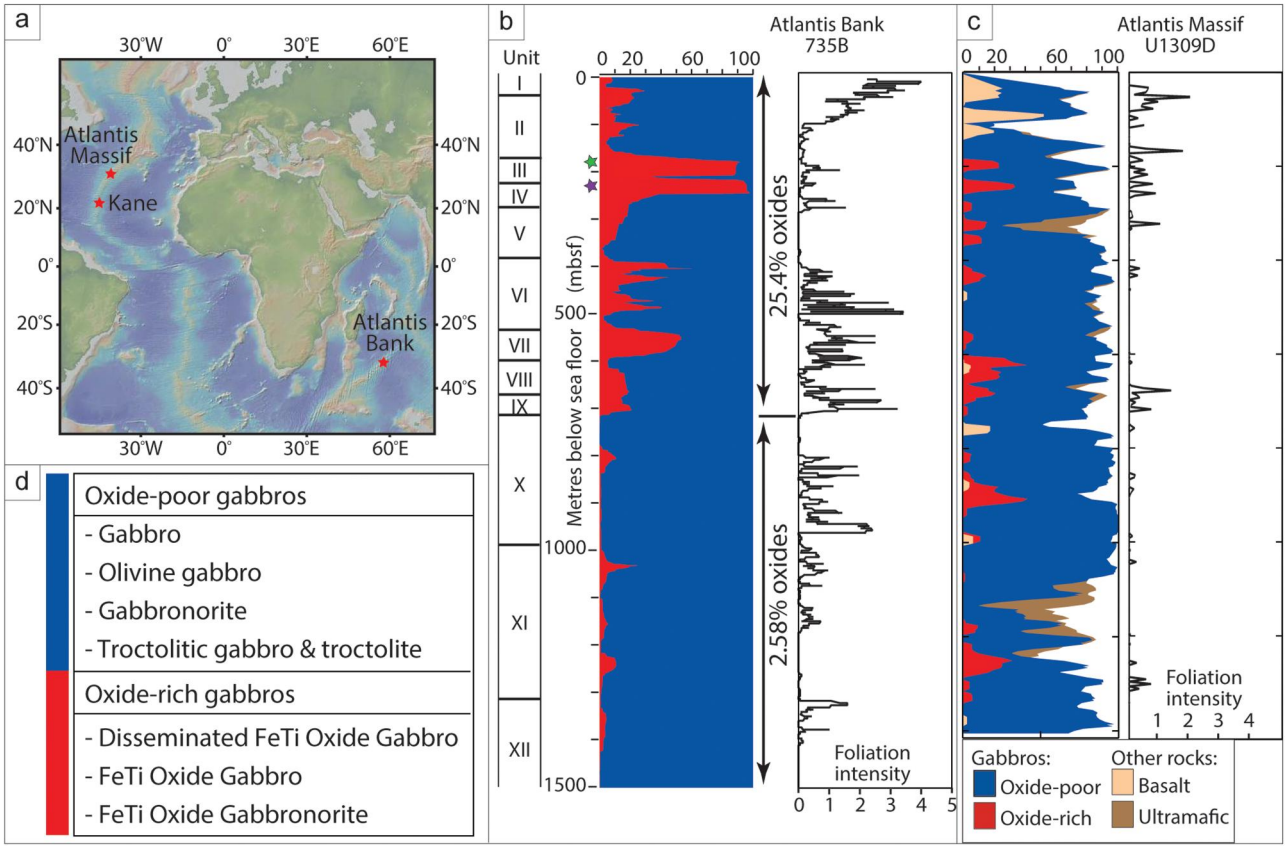

Figure 1. Sample location, oxide-poor and oxide-rich gabbro definition with simplified core lithology logs. (a) Core complex locations on South West Indian Ridge and Mid Atlantic Ridge. (b) Simplified lithology and foliation intensity from Atlantis Bank core 735B, modified from Dick *et al.* (1999b). (c) Simplified lithology and foliation intensity of Atlantis Massif core U1309D, modified from Blackman and Expedition Scientists (2006) where similar methods for calculating averages were undertaken. Rocks categorised as 'other' are ultramafic rock types including dunite, wehrlite and harzburgite. (d) Gabbro rock types included in the oxide-rich and oxide-poor simplified lithologies. Lithology was taken from a running average over 20 m intervals; stars indicate depths for samples 38R4 and 46R1; foliation intensity (from an '11 cell' or '1–2 m visual average'/5 m running average); 0, undeformed/absent; 1, weakly foliated/local nests of neoblasts; 2, strongly foliated/10% neoblasts; 3, porphyroclastic, protomylonite/40–90% neoblasts; 4, strongly laminated, mylonite/mylonitic with rare porphyroclasts; 5, ultramylonite/ultramylonitic (Dick *et al.*, 1999b; Blackman *et al.*, 2006a).

the core (Figure 1b). At a newly drilled core (Leg 118, U1473A, 789.7 m) on the Atlantis Bank, in 1–2 km from core 735B, MacLeod *et al.* (2017) recognised a ~600 m-thick high temperature shear zone at the top of the core and some narrow shear zones within the relatively undeformed deeper core. The shipboard team (MacLeod *et al.*, 2017) found the rock units of 735B and U1473A could not be directly correlated.

Recently, Zhang *et al.* (2020) recognised two styles of consecutive melt migration and melt–rock interaction at Atlantis Bank by using mineral trace element compositions: (1) early diffuse migration of a high-temperature oxide-undersaturated fractionated gabbroic melt released during compaction of a crystal mush, that is, pervasive compaction-driven transport of interstitial melts; overprinted by (2) migration of a lower-temperature oxide-saturated melt in shear zones. Similarly, Boulanger *et al.* (2020) recognised ubiquitous diffuse reactive porous flow of a compaction-derived melt in the grainsize-layered gabbro they investigated from Unit VII of core 735B. The link between deformation, melt migration and oxide enrichment in the shear zone studied by Zhang *et al.* (2020) is confirmed by the microstructural study of Ghatak *et al.* (2022), who concluded that high modes of ilmenite and magnetite in the rocks were due to high time-integrated melt flux of oxide-saturated melts that drove melt–rock interactions causing the increase in the mode of oxides.

Gardner *et al.* (2020) and Zhang *et al.* (2020) showed that the major element compositions of minerals in their melt-fluxed shear zones overlap the undeformed rocks but also shift to lower X_{An} in plagioclase and lower X_{Mg} in olivine, orthopyroxene and clinopyroxene, similar to, but less extreme in extent than, the patterns recognised in oxide-rich samples by Ghatak *et al.* (2022). Throughout the entire core, oxide-rich gabbros show the lowest X_{An} in plagioclase and lowest X_{Mg} in ferro-magnesium minerals. Together, these detailed geochemical and microstructural studies link deformation-assisted melt migration of an oxide-saturated melt with lower X_{An} in plagioclase and lower X_{Mg} in olivine, orthopyroxene and clinopyroxene in metasomatised gabbroic rocks.

Atlantis Massif and MARK (Mid-Atlantic Ridge)

The Atlantis Massif oceanic core complex lies at the ridge–transform intersection, adjacent to the Mid-Atlantic Ridge (MAR, Figure 1a) and the Atlantis transform. The core complex is approximately 16 km long and 8–10 km wide. The U1309D drilled core (30°10.12′N, 42°07.11′W) was drilled to 1415.5 mbsf on IODP expeditions 304 and 305, with a recovery rate of ∼75% (Figure 1c). The variety of rocks drilled is similar to that of Atlantis Bank but also includes ultramafics and basalt. The shipboard party defined the foliation intensity (Figure 1b) by observation: 0, undeformed; to 5, ultramylonitic. Approximately 22% of the core has a magmatic foliation, while 3% is strongly foliated or mylonitic at the core scale. A number of studies interpret extensive melt–rock interaction in olivine-rich trocolites that comprise 5.4% of the U1309D core (*e.g.* Drouin *et al.*, 2010; Ferrando *et al.*, 2018). In addition, Whattam *et al.* (2022) found that melt–rock interactions predominated on the carapace closer to the current detachment than the water–rock interaction interpreted in rocks further from the detachment.

Also on the Mid-Atlantic Ridge and adjacent to the Kane Transform (MARK area) is an intersection massif (*i.e.* core complex) approximately 15 km long and 8–10 km wide. A number of shallow cores, 921–924, were drilled during IODP expedition 153 (23°32′N, 45°01′W). The variety of rock types is again similar to Atlantis Bank, with both oxide-rich and oxide-poor rocks. The degree of crystal plastic deformation was logged by observing the percentage of recrystalised plagioclase: textural type 1, 0%; 2, <30%; 3, 30–79%; 4, 70–90%; and 5, >90% (Cannat *et al.*, 1995). These correspond to the undeformed to ultramylonitic criteria of the other cores examined here. Deformation was found to be common, occurring at high-temperature, in nearly anhydrous conditions and also in melt-present shear zones (Cannat *et al.*, 1997). Oxides were also found to be common in distinct bands, in shear zones and in pressure shadows (Agar & Lloyd, 1997). Similar to Zhang *et al.* (2020), the oxide-rich rocks at MARK have been related to migration of a lower-temperature oxide-saturated melt in shear zones (Agar & Lloyd, 1997).

Methods

Sample and data selection

The legacy whole-rock and mineral chemistry of three oceanic core complex sites was used for this analysis: (1) core 735B from IODP legs 118 and 176 on Atlantis Bank, SWIR (32°43.392′S, 57°15.960′E) drilled to 1508.0 mbsf; (2) core U1309D from IODP legs 304 and 305 on Atlantis Massif, MAR (30°10.12′N, 42°7.11′W) drilled to 1415.5 mbsf; and (3) a series of shallow cores 921–923 from ODP leg 153 in the MARK area (23°32 N, 45°01 W) drilled to between 14.6 and 82.6 mbsf. The microstructures of six samples of oxide-rich gabbro were examined from these cores: two previously examined samples from Atlantis Bank, 148R2 (Gardner *et al.*, 2020, 953.7 mbsf) and 47R2-1 (Ghatak *et al.*, 2022, 228 mbsf); two legacy samples from Atlantis Massif core U1309D (∼1300 mbsf), 270R3-1 and 279R3-2 (Blackman *et al.*, 2006b, thin sectons #640 and #641); and two new samples from the MARK area, one from core 923A: 2R2-2 (17.9 mbsf) and the second from core 921B: 3R1 (24.9 mbsf).

In addition, two oxide-poor olivine gabbro samples were analysed in detail from core 735B: (1) 46R1 (∼222 mbsf) from within the oxide gabbro of Unit IV (Figure 1b, purple star, 2) and (2) 38R4 (∼185 mbsf), from within the layered disseminated oxide gabbro of Unit III, which has grainsize layering dipping 40–50° (Figure 1b, green star, 3).

Petrography

A petrographic microscope was used on polished thin-sections for sample mineral observations. We use mineral abbreviations following Whitney and Evans (2010). A high-resolution image of the thin-sections and other associated data can be examined online in ImageMatrix at: https://imagematrix.science.mq.edu.au; search using ODP_<core#>, *e.g.* ODP_735B.

Backscatter electron imaging (BSE)

Further identification of minerals and their microstructure was undertaken using BSE images of polished thin-sections imaged on an FEI Field Emission Scanning Electron Microscope at Macquarie GeoAnalytical, Macquarie University. The operating conditions of the SEM were a high vacuum, 15 kV accelerating voltage and a dwell time of 3 μs.

Electron microprobe (EMP)

Spot analyses for the new oxide-poor samples 46R1 and 38R4 and a compositional map for sample 46R1 were acquired using a JEOL JXA 8530 F Plus electron microprobe equipped with five wavelength-dispersive spectrometers at the Central Science Laboratory, University of Tasmania. For pyroxene analyses, the beam current was 20 nA, and the beam diameter was 5 μm; for olivine and oxide minerals, it was 30 nA/2 μm; and for amphibole and plagioclase, it was 10 nA/10 μm. For the EMP compositional map, the beam current was 20 nA, and the beam diameter was 5 μm, with a dwell time of 100 ms. Previously published data were used for two of the six oxide-rich samples: 148R2 (Gardner *et al.*, 2020) and 47R2-1 (Ghatak *et al.*, 2022).

ODP legacy micro-chemical data

The ODP legacy shipboard whole-rock and mineral chemistry data from core 735B from IODP legs 118 and 176 (Dick *et al.*, 2002), core U1309D from legs 304 and 305 (Blackman *et al.*, 2006b) and cores from sites 921 to 923 from leg 153 (Cannat *et al.*, 1995) have been reclassified by rock type (Figure 1d) into (i) oxide-poor, 86% of retrieved core for both 735B and U1309D, and (ii) oxide-rich, 14% for

core 735B and 6.5% for core U1309D (per Gardner *et al.*, 2020; Ghatak *et al.*, 2022). These data have been replotted to create depth logs of (1) TiO_2 for whole rock, (2) X_{Mg} [$X_{Mg} = 100 \times Mg / (Mg + Fe)$], based on 85% FeO, for whole rock, olivine, orthopyroxene and clinopyroxene, and (3) X_{An} [$X_{An} = 100 \times Ca / (Ca + Na + K)$] for plagioclase.

Results

Detailed microstructure of representative samples

Oxide-poor samples at Atlantis Bank

Two visually and microstructurally dissimilar samples of olivine gabbro, 38R4 and 46R1, representative of low oxide mode samples in units III and IV, respectively, have been chosen to investigate microstructure. The first sample, 46R1, has little foliation and is cut by olivine-rich bands (Figure 2). The second sample, 38R4, has a strong foliation and shows grainsize layering (Figure 3).

Weakly foliated sample: 46R1 (from Unit IV—222 mbsf, SWIR core 735B)

Sample 46R1 (Figure 1b, 2) is composed of plagioclase (~67 vol%), diopside (~22 vol%), olivine (~9 vol%) and oxides (~1 vol%) with minor enstatite and amphibole. The olivine occurs in bands of rock (2–3 mm wide), oriented at approximately 40° to the weak foliation (Figure 2a).

Outside the olivine-rich bands, plagioclase and diopside grainsize is generally coarse (1–2.5 mm, up to > 4.5 mm), commonly displaying undulose extinction and deformation twinning (Figure 2b). Grain shapes are irregular. Diopside grains commonly have thin lamellae of enstatite (Di_1, Figure 2a inset). In contrast, within the olivine-rich bands, grainsizes are smaller (<0.5 mm), yet plagioclase grains still display undulose extinction and deformation twinning (Figure 2b, d). Larger diopside grains also commonly have thin lamellae of enstatite (Di_1, Figure 2e), whereas rim domains and finer grains do not (Di_2, Figure 2e).

Olivine occurs in bands of rock as irregular-shaped grains with variable size (<10 μm to ~1.8 mm). Olivine is commonly associated with fine-grained enstatite, diopside (Di_2, lacking lamellae of enstatite), plagioclase and oxides (Figure 2a–e). Within the bands, olivine is the predominant ferro-magnesium mineral. It commonly has concave boundaries and low apparent dihedral angles on triple junctions with plagioclase and/or diopside (Figure 2c, d).

Oxides, to 0.5 mm, are predominantly ilmenite and magnetite. Magnetite has very fine inclusions of ilmenite and spinel, and appears dusty in the BSE images. Ilmenite, by contrast, is cleaner and hosts a string of spinel grains on the interface with magnetite (Figure 2f).

Strongly foliated sample: 38R4 (from Unit III—185 mbsf, SWIR core 735B)

Sample 38R4 (Figure 1b, 3) can be divided into two domains, one finer grained than the other, although mineral associations and microstructures are similar (Figure 3). It has a strong foliation in both fine-grained and coarse-grained areas (Figure 2a) and is composed of plagioclase (~55 vol%), diopside (~37 vol%), olivine (~7.5 vol%) and oxides (~0.5 vol%), and with minor enstatite and amphibole.

Plagioclase and diopside grainsizes are variable up to >3.7 mm and with large grains displaying undulose extinction (Figure 3d, g). Additionally, coarse plagioclase displays deformation twins (Figure 3d, g). Grain shapes are elongate and irregular forming the foliation. Larger diopside grains commonly have thin lamellae and in places larger inclusions of enstatite (Di_1, Figure 3b, e, inset), whereas rim domains and finer grains do not (Di_2, Figure 3b, c, f). Fine plagioclase and diopside have highly irregular shapes.

Olivine occurs as irregular-shaped, highly elongate, smaller grains with variable size (<10 μm to ~0.25 mm). Olivine is most common between plagioclase and diopside (Di_2), associated with minor fine-grained oxide (Figure 3e–g) and enstatite (Figure 3b, c, e, f). Some olivine grains occur in the strain shadows of and/or asymmetrically on diopside (Di_2, Figure 3a). Olivine grains in the strain shadows are commonly single crystals with optically continuous fingers into diopside (Di_1, Figure 3b, inset). Larger, irregular-shaped grains of olivine (~50 μm to 2.5 mm) are also associated with diopside (Figure 3a), with some displaying undulose extinction (Figure 3d). The olivine and associated oxide and enstatite grains commonly have concave boundaries (Figure 3e–g) and low apparent dihedral angles on triple junctions with plagioclase and/or diopside (Figure 3b, c, e, f). Some elongate and irregular-shaped grains are optically continuous (Figure 3g).

Oxide-rich samples across three oceanic core complexes

Fine-grained and coarse-grained oxide-rich samples are examined from cores in the Indian Ocean (SWIR) and the Atlantic Ocean (MAR and MARK).

Fine-grained oxide-rich samples

Weakly foliated sample: 148R2 (from Unit X—953.7 mbsf, SWIR core 735B)

Sample 148R2 (Figure 4a) has a weak foliation and is composed of plagioclase, diopside, olivine and fine-grained oxides, with minor enstatite and hornblende. Plagioclase and diopside have irregular grain shapes, and grainsize is variable up to 2 mm. Plagioclase displays undulose extinction (orange arrows), with large grains also displaying deformation twins (yellow arrows). The smallest plagioclase grains (brown arrows) are associated with fine grains of olivine, oxides and pyroxenes forming strings, which delineate the foliation, through the sample. The oxides, olivine and enstatite grains commonly form films along grain boundaries (dark green arrows) and subtend low apparent dihedral angles on triple junctions with plagioclase and/or

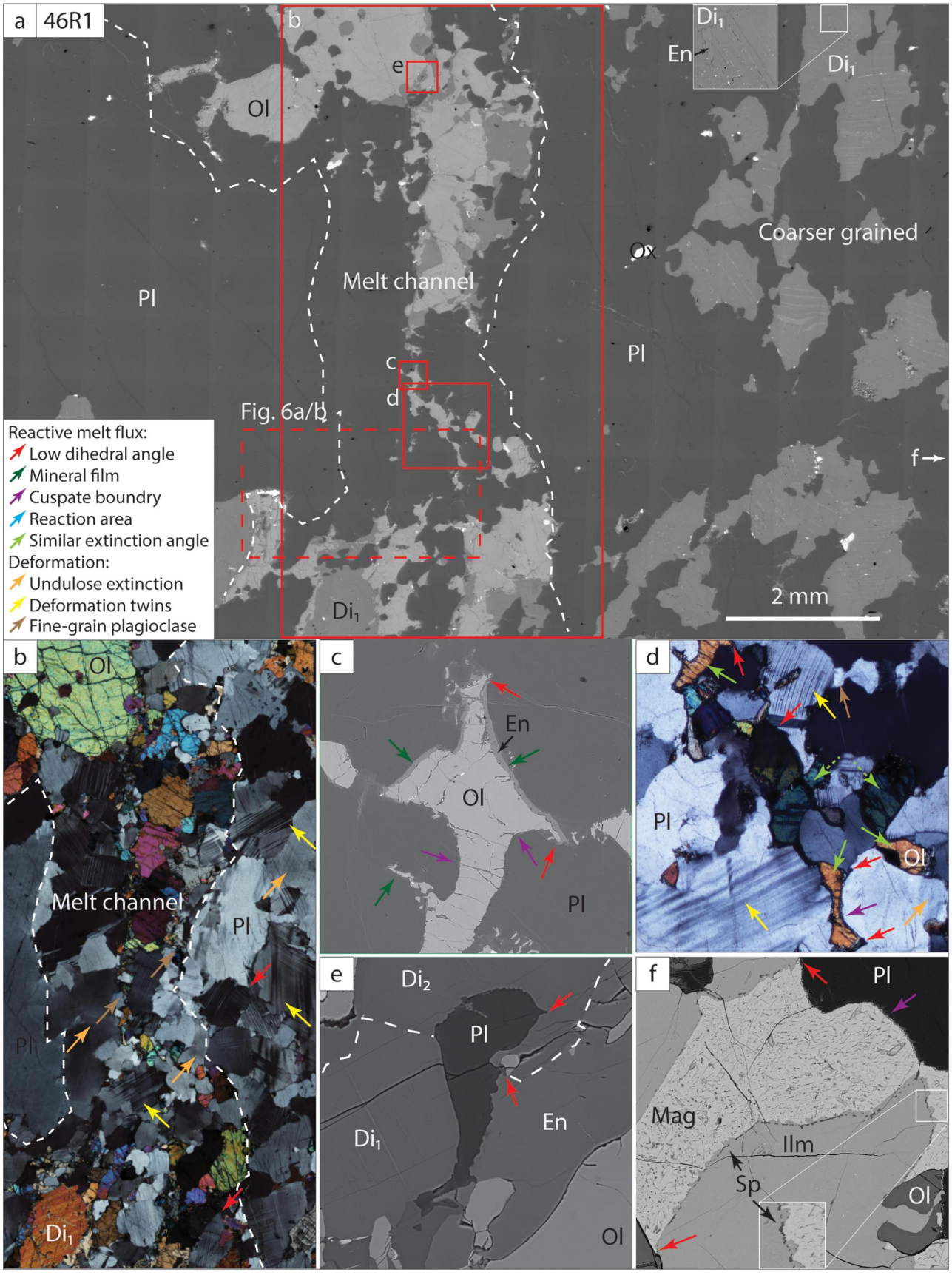
a
46R1
b
e
Ol
Di1
En
Di1
Coarser grained
Ox
Melt channel
Pl
Pl
c
d
Fig. 6a/b
f
Reactive melt flux:
Low dihedral angle
Mineral film
Cuspate boundry
Reaction area
Similar extinction angle
Deformation:
Undulose extinction
Deformation twins
Fine-grain plagioclase
Di1
2 mm
b
Ol
Melt channel
Pl
Pl
Di1
c
En
Ol
Pl
d
Pl
Ol
e
Di2
Pl
En
Di1
Ol
f
Pl
Mag
Ilm
Sp
Ol

diopside (red arrows). All minerals display some cuspate boundaries (purple arrows). The very fine-grained oxide, olivine, plagioclase and enstatite form intergrown aggregations that are inferred to be sites of previous reactions (light blue arrows). Olivine also has some irregular-shaped grains that are optically continuous (light green arrows).

Banded fine- and coarse-grained sample: 2R2-2 (from Unit 1—17.9 mbsf, MARK core 923A)

Sample 2R2-2 (Figure 4b) is an oxide gabbro sample from unit 1, which is a variably deformed gabbro and olivine gabbro unit (Agar *et al.*, 1997). It has two bands, one with coarse mineral grains (to 6 mm), not shown in Figure 4b, and the other a fine-grained zone with a very strong foliation. Both zones are composed of plagioclase, diopside and oxides with minor olivine, enstatite and hornblende. In the fine-grained zone (Figure 4b), plagioclase grains (to >0.8 mm) have irregular grain shapes and display undulose extinction (orange arrows) and minor deformation twinning (yellow arrows). The smallest plagioclase grains (brown arrows) are near grains of coarse diopside (to 3.5 mm). The oxides commonly form films along grain boundaries (dark green arrows) and subtend low apparent dihedral angles on triple junctions with plagioclase and/or diopside (red arrows). All minerals display some cuspate boundaries (purple arrows). The very fine-grained oxide and plagioclase form intergrown aggregations that are inferred to be sites of previous reactions (light blue arrows and inset). Diopside also has some irregular-shaped grains that are optically continuous (light green arrows). Olivine occurs in the strain shadows of elongate, coarse diopside in the coarse-grained domain of the thin-section and is less common in the fine-grained domain.

Heterogeneous sample: 270R3-2 (from unit 3—1300.4 mbsf, MAR core U1309D)

270R3-2 (Figure 4c) is an oxide gabbro sample from the lower 'igneous unit' (of Ildefonse *et al.*, 2006) or structural unit 3 (of Blackman *et al.*, 2006a) in core U1309D of Atlantis Massif. It is composed of plagioclase, diopside and oxides with minor enstatite and hornblende. Plagioclase grainsize is bimodal. Very large plagioclase grains (to >7 mm) have tabular euhedral grain shapes, with both growth and deformation twinning (yellow arrows), and also show undulose extinction. Coarse plagioclase is in an extensive matrix of small plagioclase grains (to 0.3 mm) that have irregular grain shapes and display undulose extinction (orange arrows). The small plagioclase grains (brown arrows) are associated with fine grains of diopside adjacent to larger diopsides. The oxides commonly form films along grain boundaries (dark green arrows) and subtend low apparent dihedral angles on triple junctions with plagioclase and/or diopside (red arrows). All minerals display some cuspate boundaries (purple arrows). The very fine-grained oxide and plagioclase form intergrown aggregates that are inferred to be sites of previous reactions (light blue arrows). Diopside also has some irregular-shaped grains that are optically continuous (light green arrows).

Coarse-grained oxide-rich samples

Isotropic sample: 47R2-1 (from Unit IV—228 mbsf, SWIR core 735B)

Sample 47R2-1 (Figure 5a) is an oxide gabbro that largely lacks a foliation and is composed of coarse-grained oxides with plagioclase, diopside, enstatite and minor hornblende. Plagioclase, diopside and enstatite all have irregular grain shapes with variable size to 10 mm. Plagioclase displays undulose extinction (orange arrows), with large grains also displaying deformation twins (yellow arrows). The smallest plagioclase grains are associated with fine-grained oxides and pyroxenes. The oxides and enstatite grains commonly form films along grain boundaries (dark green arrows) and subtend low apparent dihedral angles on triple junctions with plagioclase and/or diopside (red arrows). All minerals display some cuspate boundaries (purple arrows). The very fine-grained oxide, plagioclase and enstatite form intergrown aggregations that are inferred to be sites of previous reactions (light blue arrows). Enstatite has inclusions of diopside that are optically continuous with adjacent diopside (light green arrows).

Weakly to moderately foliated sample: 3R1 (from Unit 3—17.9 mbsf, MARK core 921B)

Sample 3R1 (Figure 5b) is an oxide gabbro from unit 3 that is a poikilitic olivine gabbro and troctolite unit (Agar *et al.*, 1997). It has a weak to moderate foliation and is composed of plagioclase, diopside and oxides, with minor enstatite and hornblende. Plagioclase grainsize is bimodal. Very large plagioclase grains (to >10 mm) have elongated grain shapes, which delineate the foliation, with both deformation twinning (yellow arrows) and undulose extinction. Small plagioclase grains (to 0.3 mm) have irregular grain shapes and display undulose extinction (orange arrows). The smallest plagioclase grains (brown arrows) occur near the coarse diopside (to 6 mm), plagioclase and oxide grains. Fine plagioclase grains are also associated with fine grains

Figure 2. Microstructures indicative of former melt presence for sample 46R1. (a) Back-scattered electron (BSE) overview of sample showing coarse-grained zone cut by a fine-grained channel. (b–e) Channel: (b) Crossed-polarised light (XPL) photomicrograph of channel showing fine grainsizes; (c) BSE image showing microstructures as indicated; (d) XPL photomicrograph showing deformation microstructures of bent deformation twins and undulose extinction in Pl and two sets (light green arrows, dashed and solid) of Ol grains of similar extinction angle inferred to be two single Ol grains in 3D; and (e) BSE image showing reaction products of Ol, En and Di_2. (f) BSE image of oxide reaction front from coarse-grained zone.

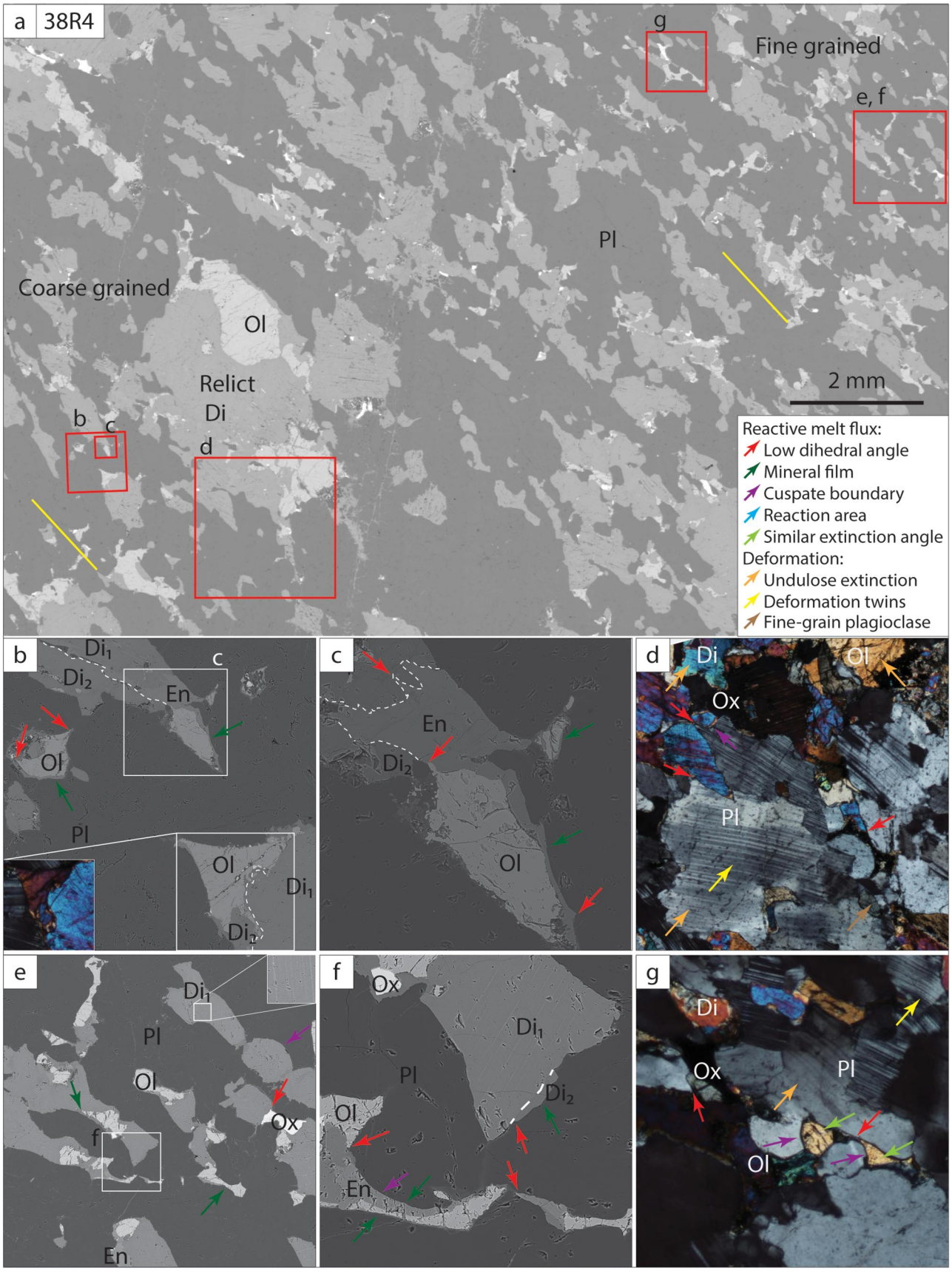
a
38R4
g
Fine grained
e, f
Pl
Coarse grained
Ol
Relict
Di
2 mm
b
c
d
Reactive melt flux:
Low dihedral angle
Mineral film
Cuspate boundary
Reaction area
Similar extinction angle
Deformation:
Undulose extinction
Deformation twins
Fine-grain plagioclase
b
Di1
Di2
c
En
Ol
Pl
Ol
Di1
Di1
c
En
Di2
Ol
d
Di
Ol
Ox
Pl
e
Di1
Pl
Ol
Ox
f
En
f
Ox
Di1
Pl
Di2
Ol
En
g
Di
Ox
Pl
Ol

of oxides and pyroxenes forming strings through the sample. The oxides commonly form films along grain boundaries (dark green arrows) and subtend low apparent dihedral angles on triple junctions with plagioclase and/or diopside (red arrows). All minerals display some cuspate boundaries (purple arrows). The very fine-grained oxide and plagioclase grains form intergrown aggregations inferred to be sites of previous reactions (light blue arrows).

Heterogeneous sample: 270R3-1 (from unit 3—1300.4 mbsf, MAR core U1309D)

Sample 270R3-1 (Figure 5c) is an oxide gabbro sample from the lower 'igneous unit' (of Ildefonse *et al.*, 2006) or structural unit 3 (of Blackman *et al.*, 2006a) in core U1309D from the Atlantis Massif. It is composed of plagioclase, diopside and oxides with minor enstatite and hornblende. The sample is heterogeneous, with a zone of coarse-grained minerals; plagioclase to ~9 mm, diopside to ~5 mm and oxides to ~2.5 mm. This is cut by a zone of fine-grained minerals similar to sample 270R3-2 (Figure 4c). Large plagioclase grains (to >7 mm) have irregular grain shapes, with both deformation twinning (yellow arrows) and undulose extinction. Smaller plagioclase grains (to 0.3 mm) also have irregular grain shapes and display undulose extinction (orange arrows). The small plagioclase grains (brown arrows) are associated with fine grains of diopside adjacent to larger diopsides. The oxides commonly form films along grain boundaries (dark green arrows) and subtend low apparent dihedral angles on triple junctions with plagioclase and/or diopside (red arrows). All minerals display some cuspate boundaries (purple arrows). The very fine-grained oxide and plagioclase form intergrown aggregations that are inferred to be sites of previous reactions (light blue arrows). Diopside also has some irregular-shaped grains that are optically continuous (light green arrows).

Mineral microchemistry: oxide-poor samples

The two samples analysed here from Atlantis Bank have a restricted X_{Mg} [X_{Mg} = Mg / (Mg + Fe)] with no appreciable difference between coarse and fine grains (Figure 6c). Mineral chemistry ranges are for olivine X_{Mg} = 0.53–0.56, enstatite X_{Mg} = 0.62–0.66 and diopside X_{Mg} = 0.69–0.74 (Figure 6c).

Plagioclase (Figure 6d) has a limited X_{An} = 0.41–0.45 [X_{An} = Ca / (Ca + Na + K)] for bimodal, foliated sample 38R4 and a broader range of 0.39–0.72 for sample 46R1 (which has the olivine-rich channels). The greatest variability in plagioclase composition is observed in the olivine-rich bands in sample 46R1 (Figure 6d, circles), with most analyses across the sample being andesine in composition. Although the fine-grained plagioclase in the olivine-rich bands (Figure 6a, b, d, dark blue triangles) is predominantly andesine (Figure 6d, open circles), the grains are zoned to higher X_{An} values asymmetrically on the rims (Figure 6b, *e.g.* black arrow), extending to labradorite and bytownite compositions (Figure 6a, b, d, orange triangles).

The observed relatively homogeneous mineral chemistry matches the legacy mineral chemistry data for oxide-rich gabbro at the equivalent depths in the core and is provided to place the microstructural and chemical observations above into the broader context of the legacy mineral chemistry data (Figure 7f).

Legacy mineral chemistry

SWIR 735B core, Atlantis Bank

Using our simplified rock classification of two groups based on oxide content (Figure 1d), overall, the core has ~86 vol% gabbro and 14 vol% oxide-rich gabbros (Figure 1b). However, the top half of the core has a higher proportion of oxide-rich rocks (25.4 vol%) than the bottom half (2.58 vol%, Figure 1b). The plots of mineral chemistry *vs* depth coloured by oxide content (Figure 7c–f) indicate that deep in the core, there is little variation of olivine, orthopyroxene, clinopyroxene and plagioclase composition between the oxide-rich and oxide-poor rock groups. Lower in the core (>950 mbsf), olivine X_{Mg} = 0.65–0.76, orthopyroxene X_{Mg} = 0.70–0.79, clinopyroxene X_{Mg} = 0.71–0.85, and plagioclase X_{An} = 0.47–0.64. However, in the upper sections of the core (<950 mbsf), oxide-rich samples can be broadly separated from oxide-poor samples by mineral chemistry. In the case of olivine, orthopyroxene and clinopyroxene the X_{Mg} values are reduced in the oxide-rich rocks (Figure 7c–e). Olivine X_{Mg} = 0.30–0.66, orthopyroxene X_{Mg} = 0.43–0.71, and clinopyroxene X_{Mg} = 0.53–0.80. By comparison, the oxide-poor gabbros in the upper core have slightly higher X_{Mg} values for all ferro-magnesium minerals than equivalent minerals in the lower core.

Similarly, plagioclase X_{An} values are generally lower in oxide-rich rocks (0.30–0.50), and the difference between oxide-poor and oxide-rich rocks is again largest in the upper core (<950 mbsf; Figure 7f). The oxide-poor gabbros in the upper section of the core have plagioclase X_{An} = 0.50–0.70. Again, this range overlaps with, but is slightly higher than, that for plagioclase in the lower core.

Figure 3. Microstructures indicative of former melt presence for sample 38R4. Yellow lines indicate the orientation of the foliation. Mineral abbreviations follow (Whitney & Evans, 2010). (a) BSE overview of sample showing coarse- and fine-grained zones; (b–d) coarse-grained zone: (b) and (c) BSE images showing reaction products of Ol, En and Di_2 and microstructures as indicated; (d) XPL photomicrographs showing deformation microstructures of bent deformation twins in Pl and undulose extinction in Ol and Pl; (e–g) fine-grained zone: (e) and (f) BSE images with microstructures indicated and (g) XPL photomicrograph matching (f) showing two grains of similar extinction angle indicating a single Ol grain connected in 3D by a film.

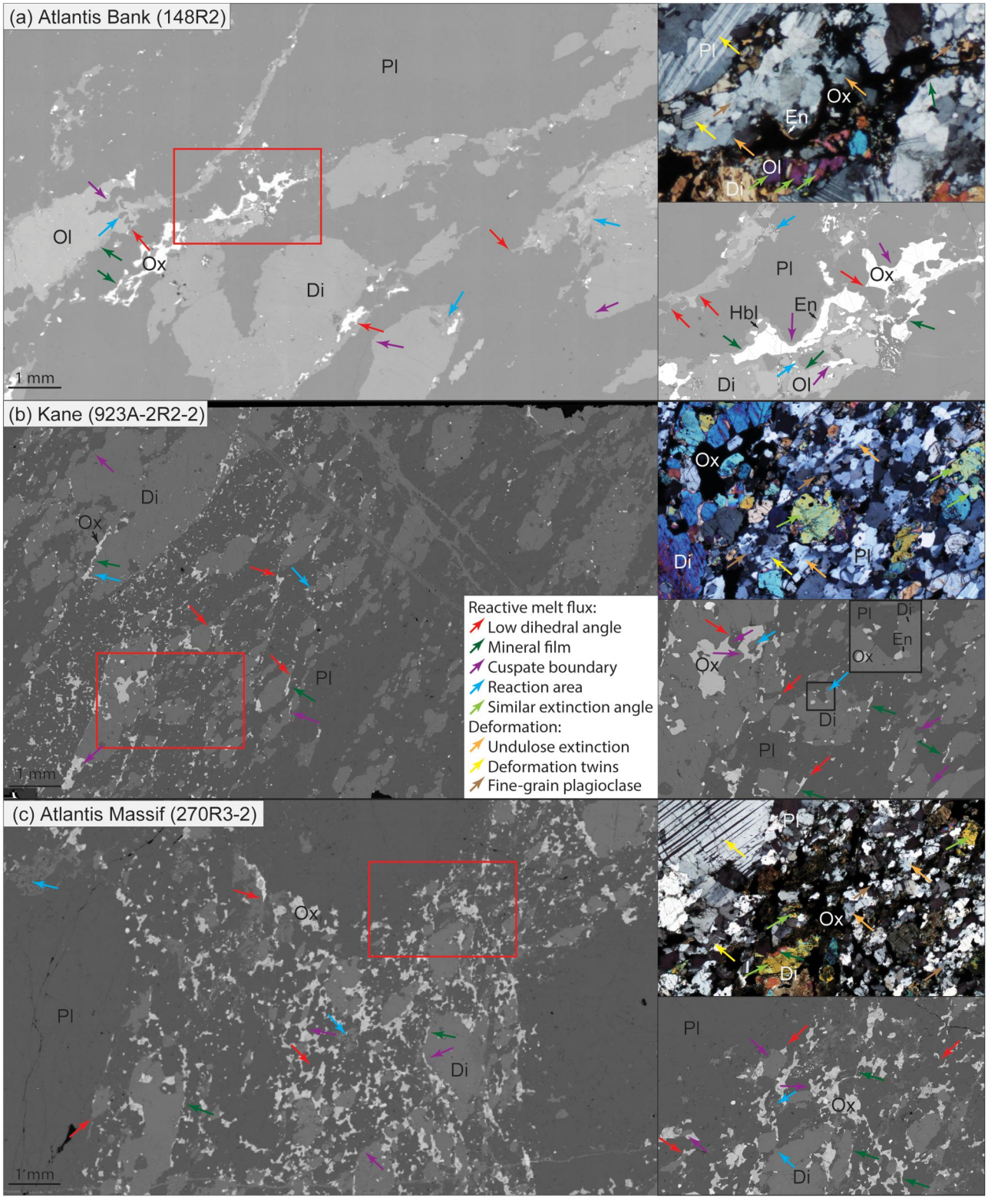

Figure 4. Fine-grained oxide sample comparison of microstructures indicative of melt–rock reactions and deformation across three oceanic core complexes (see text for details).

The lowest X_{Mg} and X_{An} values are in the oxide-rich rocks at ~260 mbsf. The difference in mineral chemistry between oxide-rich and oxide-poor rocks reduces with depth in the core. That is, the chemical pattern gradually tapers from ~280 to ~1500 mbsf (Figure 7c–f, red dotted lines). An initially steep decrease in X_{Mg} and X_{An} is evident from the base of Unit IV (~270 mbsf, oxide gabbro) to Unit III (~220 mbsf, disseminated oxide gabbro) and above.

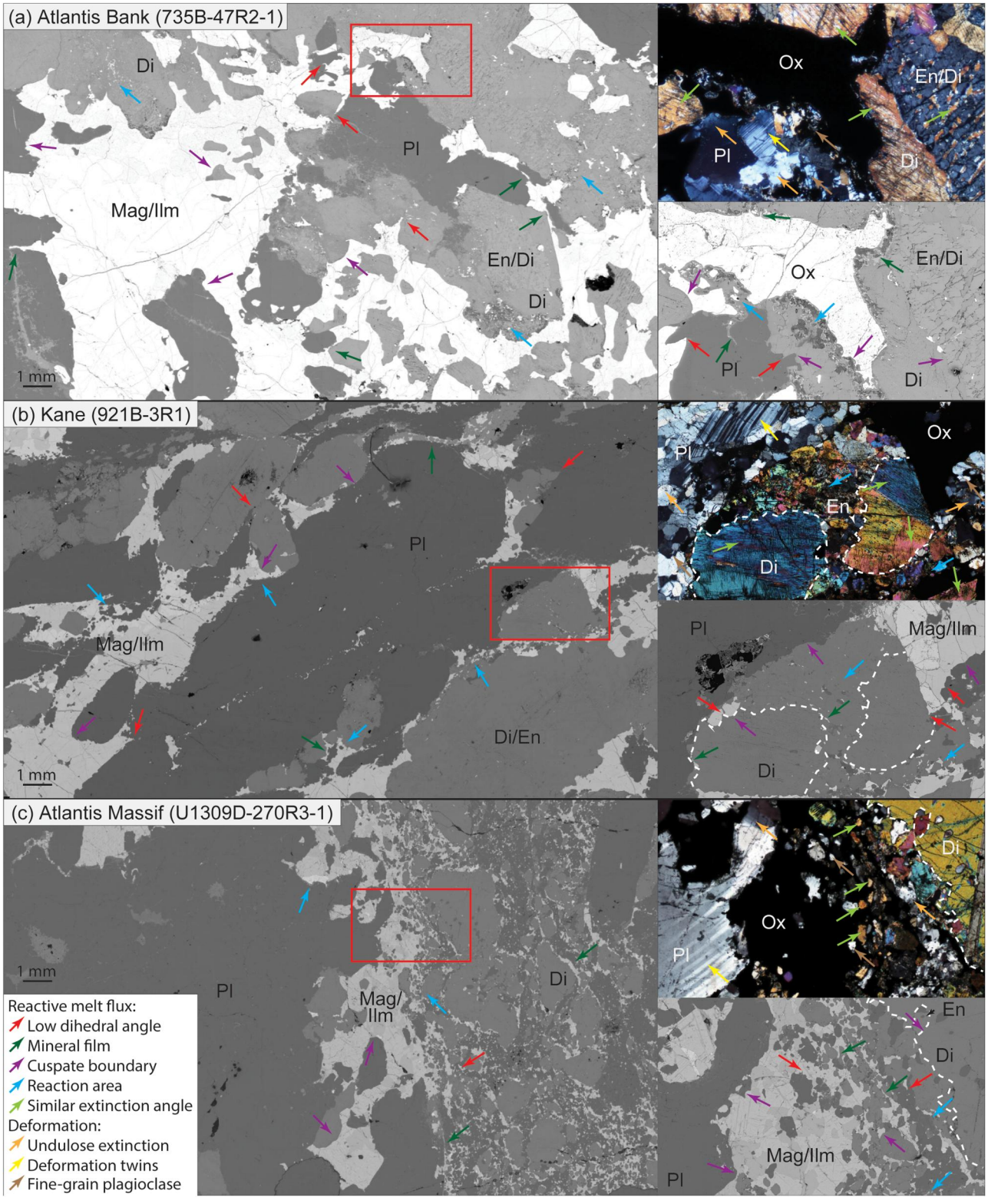

Figure 5. Coarse-grained oxide sample comparison of microstructures indicative of melt–rock reactions and deformation across three oceanic core complexes (see text for details).

Comparison with Atlantis Massif and MARK area core complexes

Using our simplified rock classification of two gabbro groups based on oxide content (Figure 1d), overall, the U1309D Atlantis Massif core has ~86 vol% gabbro, 6.5 vol% oxide-rich gabbros, 4.6 vol% ultramafics and 2.6 vol% basalt (Figure 1c). Unlike the SWIR core, there is no dominance of oxides in the top half of the core;

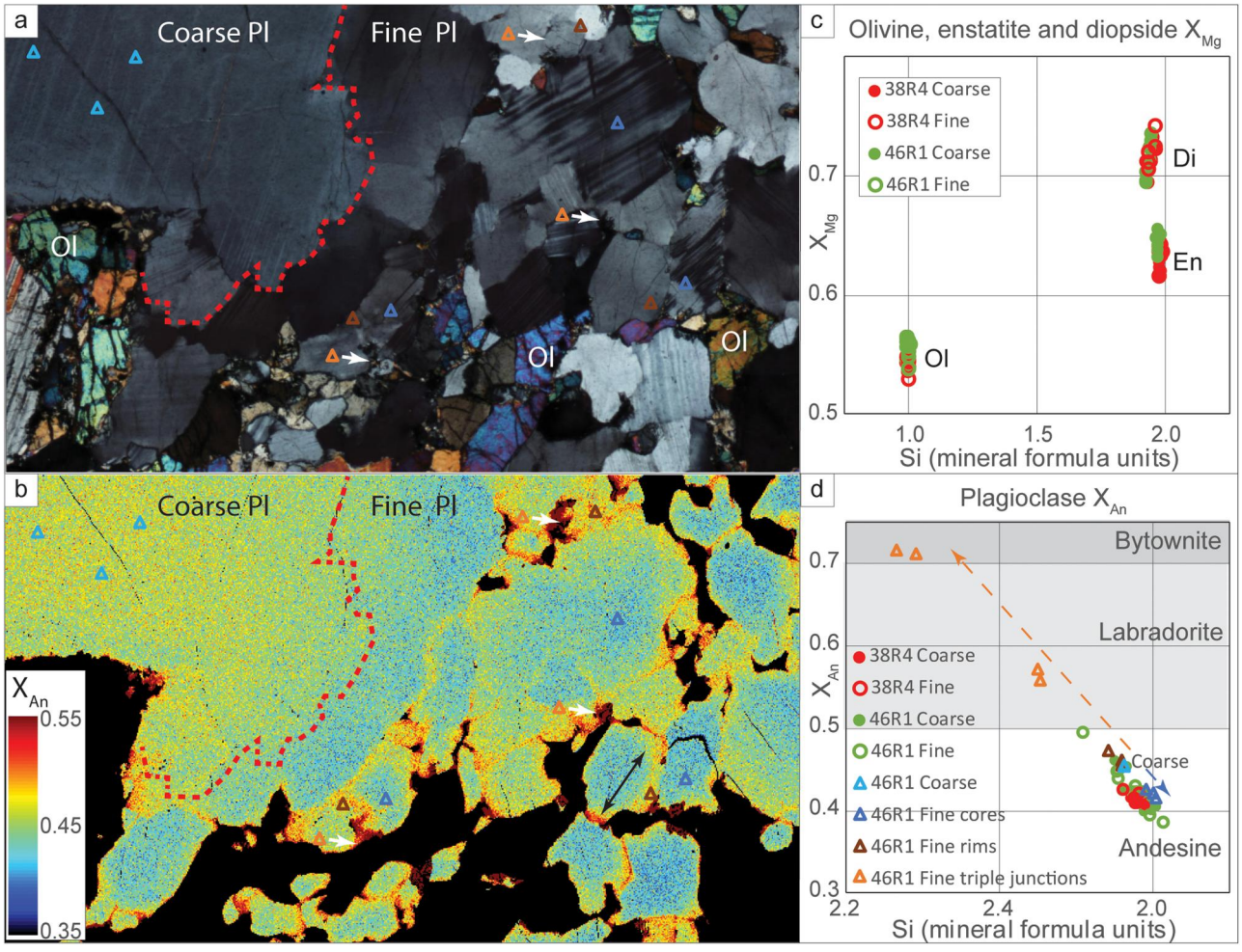

Figure 6. Olivine, enstatite, diopside and plagioclase mineral chemistry. (a) XPL photomicrograph of 46R1 sample area shown in X_{An} map in (b). (b) Map showing variation and asymmetry (black arrow) of plagioclase X_{An} across coarse (light blue triangles) and fine grains (dark blue triangles) with higher Ca content on fine grain boundaries (brown triangles) and highest Ca content on grain boundaries with olivine (orange triangles)—colour scheme is restricted to highlight subtle variations in Ca content (all values above 0.55 are brown) and compositions marked with triangles are included in (d). (c) Olivine (Ol), enstatite (En) and diopside (Di) X_{Mg} showing minor variation in composition based on grainsize. (d) Plagioclase X_{An}; circles are samples taken across the thin-section; triangles are from the map in (b); arrows show variation from original composition to fine grain triple junctions via fine grain rims (orange) and to fine grain centres (blue).

instead, the oxide-rich rocks are spread throughout the core.

Geochemical features (summarised in Table 1, with median values given after figure references in text below) common to all three sites include oxide-poor rocks (Figure 7, blue colours) with (1) relatively restricted whole-rock TiO_2 (Figure 7a; 0.35 vol%) and X_{Mg} (Figure 7b; 78), (2) relatively restricted mineral X_{Mg} for olivine (Figure 7c; 73), orthopyroxene (Figure 7d; 75) and clinopyroxene (Figure 7e; 80) and (3) variability in X_{An} (60). In contrast, the oxide-rich rocks (Figure 7, red colours) can overlap the ranges for the oxide-poor samples, but commonly have a marked increase in TiO_2 (Figure 7a; 3.28 vol%) and decrease in X_{Mg} (Figure 7b; 48) for whole rock. Additionally, ferromagnesian minerals show lower X_{Mg} for olivine (Figure 7c; 59), orthopyroxene (Figure 7d; 61) and clinopyroxene (Figure 7e; 71) and plagioclase with lower X_{An} (Figure 7f; 40).

Discussion

Microstructures indicative of deformation and the former presence of melt

All samples from the three core complexes show evidence of deformation including deformation twinning in plagioclase (yellow arrows, Figures 2b, d, 3d, g, 4 and 5) and undulose extinction, predominantly in the precursor coarse-grained minerals (orange arrows, Figures 2b, 3d, g, 4 and 5). In addition, fine-grained plagioclase (brown arrows, Figures 2b, 3d, g, 4 and 5) from recrystallisation of original grains and/or newly precipitated from melt-induced reactions are seen in all samples. This indicates all samples have undergone varying degrees of solid-state deformation.

Vernon (2011) and Daczko and Piazolo (2022) reviewed and compiled a list of reliable microstructural criteria for the former presence of melt. A comparison is provided of microstructural evidence of igneous rocks (Figure 8a), where euhedral grains are common, to melt-fluxed rocks, where

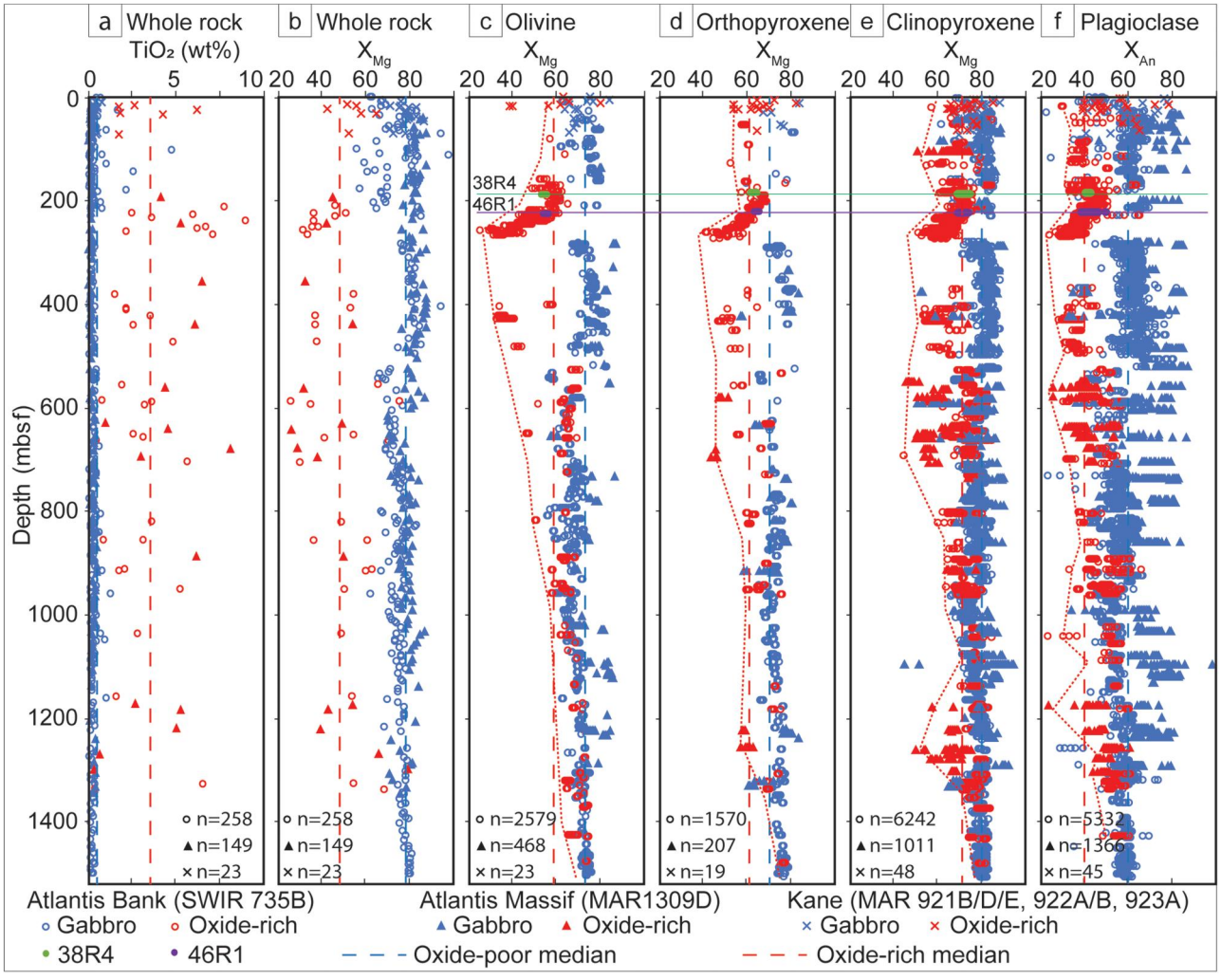

Figure 7. Comparison of oxide-poor and oxide-rich whole-rock geochemistry and mineral chemistry from Atlantis Bank, Atlantis Massif (MAR) and MARK area (MAR) with foliated and unfoliated samples from Atlantis Bank shown (SWIR; green and purple dots, depth highlighted with coloured lines). Legacy whole rock: (a) TiO_2 and (b) X_{Mg} [$X_{Mg} = 100 \times Mg/(Mg + Fe)$, based on 85% FeO] and mineral chemistry. (c), (d), (e) X_{Mg} for olivine, orthopyroxene and clinopyroxene; (f) X_{An} for plagioclase [$X_{An} = 100 \times Ca/(Ca + Na + K)$]. Data from shipboard datasets. Red dotted lines indicate first-order trends of variability of oxide-bearing samples; red and blue dashed lines are median values for oxide-rich and oxide-poor samples, respectively.

Table 1. Whole-rock and mineral chemistry summary.

	Whole rock		Mineral chemistry			
	TiO_2 vol%	X_{Mg}	Ol X_{Mg}	Opx X_{Mg}	Cpx X_{Mg}	Pl X_{An}
Oxide-poor gabbros						
735B	0.15–4.83	56–98	56–84	60–83	62–90	19–81
U1309D	0.04–0.56	70–89	57–87	57–83	44–95	19–97
Kane	0.14–0.81	71–87	71–87	67–84	68–88	39–76
Range	0.04–4.83	56–98	56–87	57–84	44–95	19–97
Average	0.39	78	73	74	80	60
Median	0.35	78	73	75	80	60
No. of samples	372	372	2333	1257	5195	4869
Oxide-rich gabbros						
735B	0.46–9.0	26–76	25–76	42–83	44–86	16–65
U1309D	0.34–8.1	26–79	–	44–63	44–77	09–58
Kane	1.76–6.25	42–65	38–80	54–82	65–86	38–77
Range	0.34–9.0	26–79	25–80	42–83	44–86	09–77
Average	3.7	47	55	62	70	41
Median	3.28	48	59	61	71	40
No. of samples	58	58	737	539	2106	1874

secondary anhedral minerals are common (Figure 8b). Here, the criteria relevant to our samples are used as evidence for the gabbros having been modified by melt–rock interaction (1) minerals that subtend to low (<60°) apparent dihedral angles (red arrows, Figures 2–5), including olivine (Figures 2c–e and 3b, c, f), enstatite (Figures 2c and 3e, f), diopside (Figure 3f), plagioclase (Figures 2d, e and 3d, g) and oxides (ilmenite, magnetite; Figures 2f and 3e); (2) films or thin elongate minerals inferred to represent former melt that has partially penetrated along grain boundaries (*i.e.* forming fingers) now pseudomorphed by olivine, enstatite and/or oxides (dark green arrows, Figures 2b–g, 3c, e, f, 4 and 5); (3) cuspate (concave outwards) grain boundaries of olivine, enstatite and plagioclase (purple arrows, Figures 2c–d, 3d–f, 4 and 5); and (4) crystal orientation data, and/or similar extinction angles have been used to identify neighbourhoods of small grains connected in 3D (*i.e.* with branching grain shapes), such as olivine and pyroxene in our samples (light green arrows, Figures 2d, 3g, 4 and 5). These are inferred to be pseudomorphs of grain boundary melt networks (Stuart *et al.*, 2018).

Our documentation of these microstructures in all the rock-forming minerals across the samples in multiple core

complexes confirms the important role of melt-present deformation in the development of the core complexes.

Reaction textures indicative of deformation-assisted open-system melt–rock interaction

Reaction textures are powerful observations used to distinguish open from closed systems. In open systems, equilibrium of the mineral phases is rarely achieved, resulting in local disequilibrium causing variable mineral assemblages (minerals can be added or removed due to the reactions) and mineral chemistry changes over short distances, which are not due to chemical growth zoning (*e.g.* Figure 6b, d).

In the case of open-system processes, such as those inferred here, many studies have highlighted the importance of reaction textures and changes to mineral assemblages that are inferred to have been mediated by melt (Daczko & Piazolo, 2022; Daczko *et al.*, 2016; Ghatak *et al.*, 2022; Meek *et al.*, 2019; Silva *et al.*, 2022; Stuart *et al.*, 2016). In general, the presence of reaction textures and the formation of secondary minerals provide additional support to the microstructural criteria (as discussed above) indicating the former presence of melt.

Formation of secondary olivine

As an example of forming secondary minerals, we contrast the olivine-rich and olivine-poor bands in sample 46R1 (Figure 2) to infer a melt-mediated reaction that forms secondary olivine with a channel of melt migration. The dominant minerals in the olivine-poor bands are diopside and plagioclase with minor enstatite and oxides (Figure 2a). The diopside in this precursor domain contains abundant lamellae and larger inclusions of enstatite along with minor oxide inclusions (Di_1, Figure 2a). Therefore, the predominant reactants in the precursor rock are diopside and plagioclase (reaction 1).

The dominant minerals in the olivine-rich bands are olivine, plagioclase and minor enstatite, diopside and oxides (Figure 2a). This secondary diopside can be distinguished by a lack of enstatite lamellae and inclusions (Di_2, Figure 2e). It is texturally difficult to separate the two generations of enstatite. Therefore, the products of the reaction are olivine, plagioclase and minor enstatite, diopside and oxides (reaction 1). We define reaction 1 as:

$$\mathrm{Di_1 + Pl_1 + Melt_1(\pm En_1 \pm Oxides_1)} \rightarrow \mathrm{Ol + Pl_2 + Di_2 + Melt_2(\pm En_2 \pm Oxides_2)} \quad (1)$$

Olivine in the foliated sample with bimodal grainsize (38R4, Figure 3) occurs in association with enstatite, lamellae-free diopside (Di_2, Figure 3c) and oxides (Figure 3b–g). This association of minerals predominantly occurs on the rims and in strain shadows of coarse diopside with lamellae (Di_1, Figure 3b, c). Based on these mineral associations and their spatial distribution, we infer the same reaction occurred in sample 38R4, but that this reaction was pervasive throughout the sample. Additionally, we use the observation of reaction products in strain shadows to infer that the melt–rock interaction was syn-tectonic.

Formation of secondary oxides

Ghatak *et al.* (2022) studied the oxide enrichment in the 735B core and identified the following melt–rock interaction reactions resulting in the crystallisation of oxides and thereby an increase in oxide mode:

$$\mathrm{En\text{–}Pl - rich\ gabbro + Melt_1 \rightarrow Rock + Di + Ilm + Melt_2} \quad (2)$$

$$\mathrm{Ilm + Di + Melt_3 \rightarrow Mag + Sp + (new)\ Di + Melt_4} \quad (3)$$

Microstructural evidence of reaction 2, that is, the formation of secondary oxides, is common to all samples (Figures 2–5), whereas reaction 3 is additionally observed outside the olivine-rich channels in sample 46R1 (Figure 2f).

Micro-chemical features of melt–rock interaction

Mineral chemistry changes during the formation of secondary olivine

Throughout the extensive literature on the 735B core, olivine is described only as a primary mineral. That is, it precipitated from the original gabbro-forming melt. The secondary character of olivine in our study is confirmed above by its microstructure (*e.g.* inferred pseudomorphs of melt, Figures 2 and 3) and microchemistry (*e.g.* low X_{Mg} values, Figure 7c–e), and its occurrence in reaction textures (reaction 1; Figures 2c, d and 3e). Some olivine grains are inferred to be direct pseudomorphs of the infiltrating melt (Figures 2c, d and 3e, f, g), but other grains are formed by replacement of diopside as part of the melt–rock reactions (reaction 1; Figure 3b, c).

Both oxide-poor samples (core 735B: 46R1 and 38R4) are from oxide-rich units in the core, even though the samples themselves are considered oxide-poor. The ferro-magnesium minerals in the samples have overlapping mineral chemistry (X_{Mg} values, Figure 6c). However, these X_{Mg} values match the oxide-rich gabbro values (Figure 7c–e, red values) rather than the oxide-poor values, indicating that these samples have modified chemistry compared with the original gabbro.

Plagioclase in the olivine-rich band (*i.e.* the inferred melt migration channel) in sample 46R1 (Figure 2) has smaller grainsizes than the adjacent plagioclase outside the channel (Figure 6a). The subtle variation in plagioclase composition highlighted by the EMP map (Figure 6b) highlights the complexity caused by melt–rock interaction during the infiltration and migration of a melt through the precursor rock. The core (Figure 6b, dark blue triangles) to rim (Figure 6b, brown triangles) variation in plagioclase chemistry suggests there is disequilibrium between the melt and rock within the channel. The shift to lower X_{An} from coarse (outside the channel) to fine (within the channel) plagioclase locally enriches the melt film/outer edge of plagioclase grains in calcium resulting in growth of labradorite

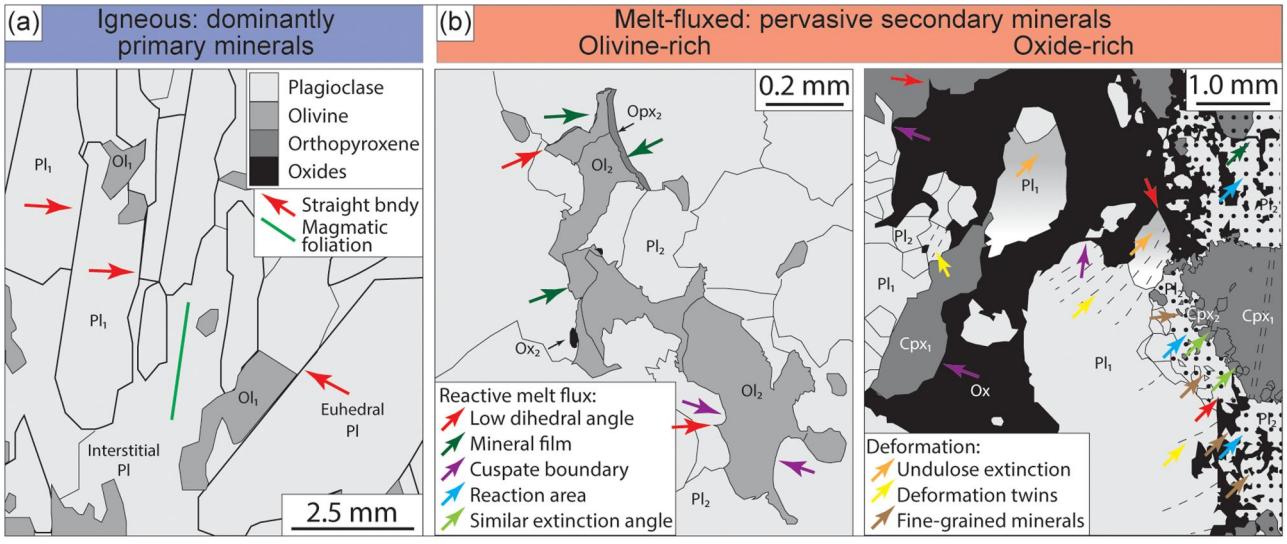

Figure 8. Microstructural evidence of secondary minerals and deformation-assisted melt migration and melt–rock interaction. (a) Example of igneous microstructures, redrawn from Deans and Yoshinobu (2019) from core 735B at 506 mbsf. (b) Examples of secondary minerals (drawn from within the olivine-rich reaction channel marked on Figure 2a, b, sample 735B-46R1) and with increasing modes of secondary oxide minerals (oxide-rich domain drawn from features in Figure 5c, sample U1309D-270R3-1); stippled area is fine-grained plagioclase.

and bytownite rims. The chemical zoning is asymmetric on the new plagioclase grains (Figure 6b, *e.g.* black arrow) suggesting that the plagioclase grains have grown and been modified in a stress regime.

The chemical composition of both fine and coarse plagioclase grains from sample 38R4 is tightly clustered close to the composition of the centres in the fine grains in sample 46R1 (Figure 6d). This suggests the 38R4 grains have completely re-equilibrated, and these now reflect reduced X_{An} melt-buffered compositions. Gardner *et al.* (2020), analysing samples lower in the core, showed that the calcium content of plagioclase decreased from labradorite in the original igneous plagioclase to andesine compositions in their S_2 shear zone. The study concluded that two generations of migrating melts were involved in the melt–rock interactions.

Secondary oxides and related mineral chemistry patterns throughout the 735B drill core

The micro-chemical patterns discussed above can be linked to macro-scale mineral chemistry trends throughout the core. Zhang *et al.* (2020) demonstrated the migration of a lower-temperature oxide-saturated melt in the shear zones examining samples from core U1473A, adjacent to core 735B, on Atlantis Bank. Additionally, in their study on high-mode (>15 vol%) oxide samples, Ghatak *et al.* (2022) showed that the high mode of oxide, 1–45 vol% oxides (Dick *et al.*, 1999a), can be a marker for melt-fluxed rocks not only in oceanic core, but also in continental rocks from central Australia. They showed that an external melt was needed to add TiO_2 to form the ilmenite present in the oxide-rich rocks. Even though both oxide-poor samples examined here have relatively low modes of oxides (~0.5–1 vol%), we interpret that the oxide minerals are predominantly secondary, as we have found similar microstructural evidence to that shown by Ghatak *et al.* (2022) (Figure 2f).

Building on the hypothesis of Ghatak *et al.* (2022) that secondary oxides delineate sites of melt migration, we reclassified the legacy mineral chemistry data from the ODP 735B core into two gabbroic rock type categories: (i) oxide-poor and (ii) oxide-rich (Figures 1b, c, d, 7 and 9). These plots show that the oxide-poor rocks have relatively restricted mineral compositions, even though Zhang *et al.* (2020) showed some of these rocks interacted with a high-temperature oxide-undersaturated fractionated gabbroic melt released during compaction of a crystal mush. In contrast, the oxide-rich rocks can overlap this restricted compositional range but commonly have a marked decrease in X_{Mg} for olivine, orthopyroxene and clinopyroxene, and in X_{An} for plagioclase, particularly in the core above ~950 mbsf (Figures 7 and 9).

Melt–rock interaction can vary between melt-buffered and rock-buffered systems dependent upon the ratio of melt to rock at any given time and the time-integrated melt flux through the rock. Together with variations in possible melt chemistry (from gabbroic to more fractionated compositions), these variables will result in diverse mineral chemistry throughout the core. This complexity is highlighted by the fact that secondary olivine is likely to have resulted from a melt distinct from the melt interacting to form the secondary oxides. Even so, our macro-scale analysis shows that the legacy data display first-order trends in mineral chemistry that can be utilised for further investigations.

Similar mineral chemistry patterns across three core complexes (Atlantis Bank, Atlantis Massif and MARK area)

The new mineral chemistry data for the two oxide-poor samples 38R4 and 46R1 at Atlantis Bank match the legacy

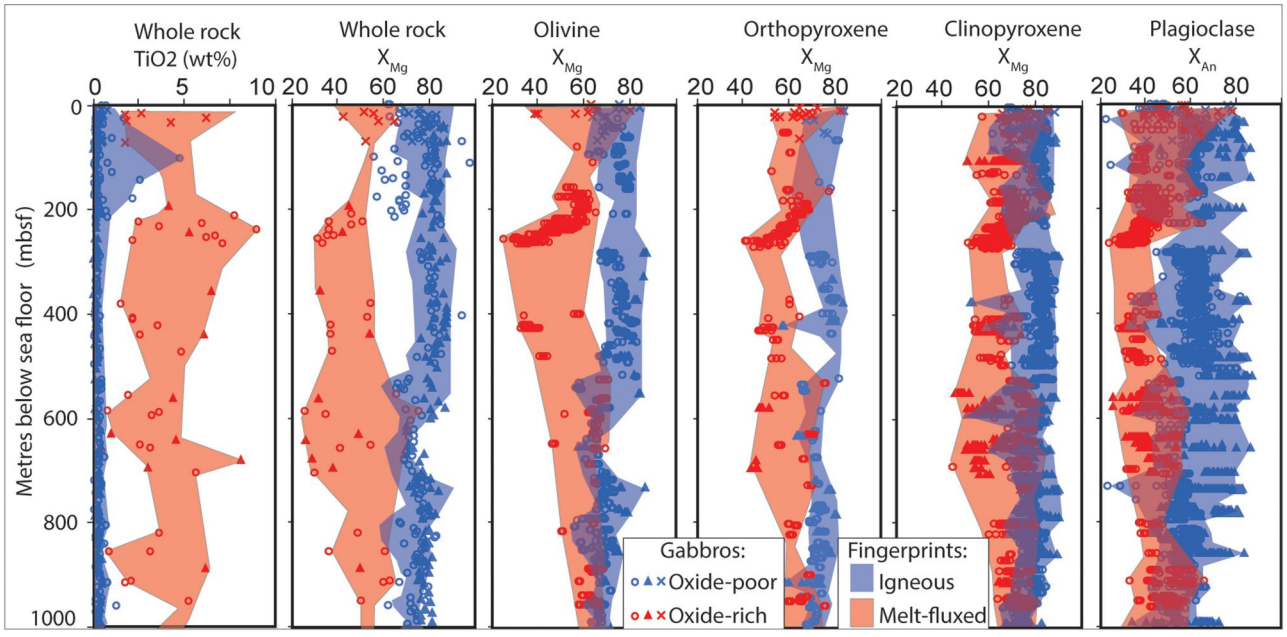

Figure 9. Kilometre-scale mineral chemistry evidence of secondary minerals. Overview of core mineral chemistry highlighting divergence of oxide-rich *vs* oxide-poor TiO_2 and X_{Mg} in whole rock and X_{Mg} in olivine, orthopyroxene and clinopyroxene and X_{An} in plagioclase across three oceanic core complexes. See Figure 7 for individual core symbol keys.

oxide-rich data collected at similar depths (Figures 1b, 6c, d and 7c–f). All detailed studies at Atlantis Bank that link microstructure and mineral chemistry, including this research, have shown that mineral chemistry shifts to lower X_{Mg} for ferro-magnesium minerals and X_{An} for plagioclase in samples inferred to have experienced melt–rock interaction (Gardner *et al.*, 2020; Ghatak *et al.*, 2022; Zhang *et al.*, 2020).

Remarkably similar patterns are seen in the Mid-Atlantic Ridge cores at Atlantis Massif and the MARK area examined here (Figures 7 and 9). In melt-fluxed oxide-rich gabbros at all three oceanic core complexes, we recognise (i) high modes of secondary oxides (Figures 4 and 5), (ii) high TiO_2 and low X_{Mg} in whole-rock geochemistry (Figures 7 and 9) and (iii) mineral chemistry patterns of decreased X_{Mg} in ferromagnesian minerals and low X_{An} in plagioclase (Figures 7 and 9). These whole-rock and mineral chemistry patterns are consistent at the kilometre scale, indicating the pervasive occurrence of secondary minerals and most likely a common process occurred at all three locations. We suggest that melt flux and melt–rock interaction have caused the formation of the secondary minerals, with their variable chemistry, across the cores. Therefore, melt-present deformation has an important role in the evolution of oceanic core complexes.

Evolution of rheological weakening of detachment faults at oceanic core complexes: solid-state and melt-present deformation

Formation of an oceanic core requires uplift of the complex on a long-lived detachment. Numerical modelling shows that strain is distributed throughout the deforming rocks if a dynamic weakening mechanism is not active and/or where the rock has high proportions (>20%) of weak components (Gardner *et al.*, 2019). Conversely, strain localises into high-strain zones, such as a core complex detachment, in rocks with small proportions (<20%) of weak components and only with concurrent dynamic weakening. In addition, the high-strain zones narrow as the weak material proportion decreases, for example, as the material cools (Gardner *et al.*, 2019). In the context of the oceanic core, this indicates that strain is distributed throughout the rocks at depth, where the rocks are hot and weak. Any strain would be accommodated by solid-state deformation, resulting in, for example, undulose extinction, deformation twins and recrystallisation in plagioclase (Figures 2–5 and 8). However, as the rocks are uplifted and cooled, the proportion of weak phase decreases, thereby forming initially wide anastomosing melt-absent shear zones that narrow as the rocks cool further. As the rocks are further uplifted and cooled past the brittle–ductile transition, deformation would transition into brittle faults.

Melt is known to weaken rocks significantly, increasing the strain rate (Hirth & Kohlstedt, 1995) and preferentially accommodating strain (Holtzman *et al.*, 2003). In addition, melt can dynamically weaken the rocks by causing reactions that result in weaker phases and/or reduced grain-sizes (*e.g.* Holyoke & Tullis, 2006). Fusseis *et al.* (2009) showed that grain boundary sliding, creep cavitation, and dissolution and precipitation processes can dynamically create a self-sustained fluid pump that can flux fluid into and through shear zones. Porous melt flow (*e.g.* Figure 3) is likely to be more prevalent in the lower, hotter rocks where little strain localisation occurs, whereas channelised melt

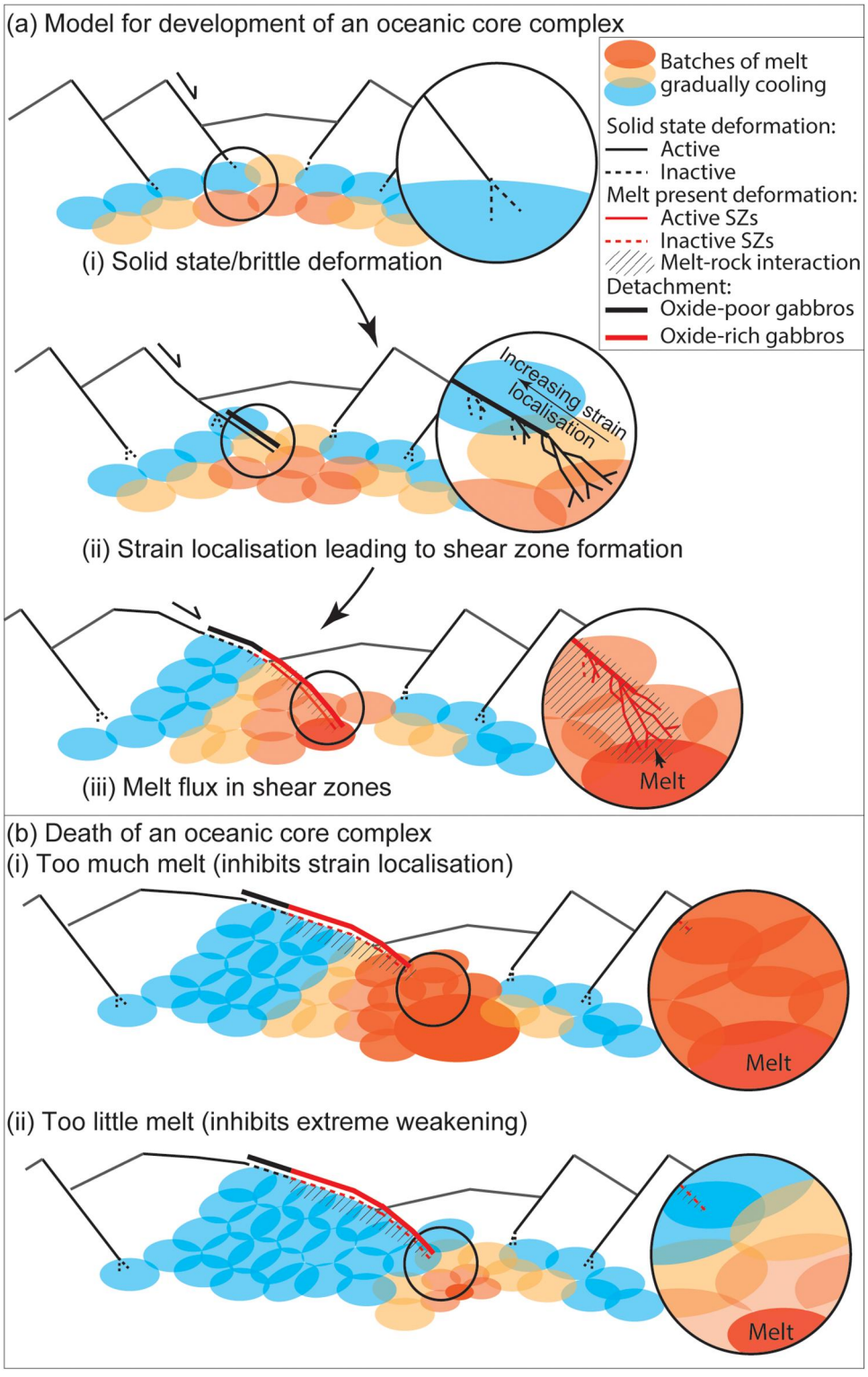

Figure 10. New model of the life and death of an oceanic core complex. (a) (i) Solid-state deformation at the mid-ocean ridge. (ii) Initiation and development of the complex due to solid-state deformation causing localisation into shear zones and the initiation of the detachment. (iii) The shear zones tap hot newly arrived melt causing lubrication and growth of the detachment while conditions continue in the goldilocks zone for the core complex growth. (b) Death of the core complex due to (i) too much melt or (ii) too little melt arriving at the ridge. Melt–rock interaction cross-hatching denotes active and previous areas of melt–rock interaction.

flow (*e.g.* Figure 2) and shear zone hosted melt flux will be more prevalent as the rocks cool, and strain localises into shear zones. Deformation-assisted melt migration in high-strain zones is increasingly recognised within oceanic core complexes (*e.g.* Casini *et al.*, 2021 and references therein; Dick *et al.*, 2019; Gardner *et al.*, 2020; Ghatak *et al.*, 2022;

Taufner *et al.*, 2021; Zhang *et al.*, 2020). As the rocks cool, evidence for each of the processes may or may not be visible in any individual rock sample, as the early processes are readily overprinted by the later processes.

A large number of microstructural studies (*e.g.* Frassi *et al.*, 2017; Gardner *et al.*, 2020; Mehl & Hirth, 2008; Miranda & John, 2010) have documented the evolution of strain in an oceanic core complex from solid-state distributed deformation (dislocation creep) to mylonites undergoing dynamic recrystallisation (dislocation creep accommodated grain boundary sliding) to ultra-mylonites undergoing further grainsize reduction (diffusion creep). Gardner *et al.* (2020) recognised that the evolution of strain localisation in the Atlantis Bank oceanic core complex began with recrystallisation during melt/fluid-absent solid-state deformation and weakening processes, then changed to reaction softening and further grainsize reduction during flux of an externally derived melt by deformation-assisted porous melt flow. They recognised that increasing time-integrated melt flux further reduced grainsize and intensified reaction softening creating a positive feedback mechanism causing additional strain localisation and melt flux. A positive feedback loop such as this is needed to create the conditions for runaway weakening and slip on the detachment and is thereby critical to the formation of the core complex.

Some researchers have suggested the lubrication of the detachment is enhanced by seawater reactions forming serpentine on the detachment (*e.g.* Dick *et al.*, 2008; MacLeod *et al.*, 2011), and we agree with this view for the shallow rocks deformed at lower temperatures. Recently, the importance of melt on the detachment has also been highlighted (*e.g.* Casini *et al.*, 2021; Taufner *et al.*, 2021). The important role of an oxide-saturated melt in the Atlantis Bank detachment is further confirmed by Dick *et al.* (2019), who mapped an oxide-rich gabbro carapace on the Atlantis Bank oceanic core complex and suggested approximately 100 m of oxide-rich gabbro had been eroded from the top of Atlantis Bank.

Life and death of an oceanic core complex—a new model

At slow- and ultra-slow-spreading ridges, gabbroic plutons are emplaced below the brittle–ductile transition zone (Frassi *et al.*, 2017). Initially the plutons are hot and melt-rich, but cool quickly due to their small scale and the cooler temperature of the lithosphere (Coogan *et al.*, 2007).

The following is a new proposal for the formation of an oceanic core complex. At first, strain is distributed throughout the hot, weak, lower crust, but with continued spreading and cooling, strain becomes accommodated by solid-state deformation at depth [dislocation creep and grainsize reduction; Figure 10a(i)] and brittle faults in the cooler upper crust. At depth, cooling causes the gradual transition of localisation into initially wide anastomosing high-strain zones, which narrow into mylonitic shear zones [diffusion creep; Figure 10a(ii)] as cooling continues. In addition, grain boundary sliding and creep cavitation cause increased porosity in the shear zones (Fusseis *et al.*, 2009).

If, at this stage, another small pluton were emplaced adjacent to or beneath the first [Figure 10a(iii)], the shear zones would tap this hot pluton creating a fluid pump (Fusseis *et al.*, 2009) causing a flux of melt through the shear zones in the original, now much cooler, pluton. This would cause localised increases in temperature and melt–rock reactions forming fine-grained products and resulting in phase mixing (Figures 2–5). A transition to grain boundary sliding and Zener pinning (Linckens *et al.*, 2015) would reduce grain growth allowing grainsizes to remain very small and thereby continuing localisation of strain into the shear zones. Fluxing melt lubricates the shear zone and allows for the formation and extreme localisation of the detachment at depth [Figure 10a(iii)]. While the melt continues to flux through the shear zone, the detachment will continue to be active, thereby allowing the uplift of the core complex [Figure 10a(iii)]. Concurrently, seawater fluxes the upper crust fault forming serpentine and talc that lubricate the fault closer to the sea floor (*e.g.* Dick *et al.*, 2008; MacLeod *et al.*, 2011).

The detachment remains active, and the core complex grows in length while the localised deformation persists, and melt continues to be available to lubricate the detachment at depth. However, uplift of the core complex would terminate if the melt-present shear zone were not maintained at depth (Figure 10b), due to either (i) too much melt, which inhibits strain localisation on the detachment [Figure 10b(i)], or (ii) too little melt, or excessive conductive cooling due to uplift and seawater infiltration, which is unable to keep the shear zone lubricated and locally heated [Figure 10b(ii)].

Dick *et al.* (2019) found evidence at Atlantis Bank of five 'upwardly differentiated olivine gabbro units' (their figure 15) all of which show evidence of oxide enrichment and strain localisation into melt-bearing shear zones. This suggests the timely emplacement of a pluton below the cooling pluton initially allows the melt to be tapped, but then as the lower pluton cools, the shear zones propagate into that lower pluton. Further uplift would allow for a cycle of pluton emplacement, melt flux and propagation of the shear zones into the new pluton as it cools [Figure 10a(iii)]. The cycle breaks down when either (i) the pluton is not emplaced before the shear zone solidifies [*i.e.* magma supply is too low; Figure 10b(ii)] or (ii) the new pluton does not cool enough to propagate the shear zone causing deformation to remain distributed throughout the pluton [*i.e.* proportions of melt are too high to localise strain; Figure 10b(i)].

This model suggests that the formation and character of an oceanic core complex are dependent on the temperature of the lower crust and the amount of magma emplaced under or adjacent to the detachment. Too much

magma causes the lower crust to be too hot, inhibiting strain localisation and the formation of shear zones. Too little magma forms a cool and strong lower crust, again inhibiting strain localisation and the formation of shear zones. Without available melt, the dynamic weakening factors discussed above are absent, limiting the growth of the detachment into younger crust and thereby terminating the lifespan of the detachment. This correlates well with numerical modelling, which shows that oceanic core complexes form when ~50% of extension at the ridge is accommodated by magma supply (Buck *et al.*, 2005), and that the location, extent and state (inactive *vs* active) of the detachment forming the oceanic core complex are controlled by temporal and lateral variation in magma supply along the axis (Howell *et al.*, 2019).

Conclusions

By combining micro-scale features with the macro-scale mineral chemical trends from ocean drilling program legacy data, we propose that the flux of variably fractionated mafic melts through detachment faults at oceanic core complexes can be recognised in three key ways: (1) high modes of secondary minerals, such as oxides and olivine, verified at the thin-section-scale (Figure 8b). The presence of secondary minerals such as the oxides is shown here to be a reliable indicator of previous melt–rock interaction (Figures 2–5 and 8); (2) microstructural evidence for the former presence of melt (Figure 8a compared with Figure 8b), including low apparent dihedral angles, films, curved boundaries between unlike minerals, grains connected in 3D, and reaction textures (Figures 2–5); and (3) mineral chemistry, specifically, reduced X_{Mg} in olivine, orthopyroxene and clinopyroxene, and reduced X_{An} in plagioclase (compare red *vs* blue shaded areas in Figure 9). Individually, each feature is indicative of a local melt–rock interaction event, but by combining micro-scale with core-scale data, we show the important role that melt-present deformation has on core complex evolution.

Our new evolutionary model for the initiation and propagation of an oceanic core complex indicates that the formation is dependent on the temperature of the lower crust and the amount of magma emplaced under or adjacent to the detachment. Too much magma causes the lower crust to be too hot and inhibits the formation of shear zones, which propagate the detachment at depth. Too little magma causes the lower crust to be too cool and reduces the amount of melt fluxing, which impedes the maintenance of strain localisation on the detachment shear zones.

Acknowledgements

The authors would like to thank Karsten Gorman of University of Tasmania for his assistance collecting the EMP data. We would also like to thank Melanie Finch and an anonymous reviewer for their constructive reviews.

Author contributions

SP and ND formulated the original concept and methodology, RG prepared the original draft and figures, and all authors reviewed the manuscript.

Disclosure statement

No potential conflict of interest was reported by the authors.

Funding

Logistical and analytical funding was provided by the Australian IODP Office (ANZIC Legacy Analytical funding AILAF_2111) and the School of Natural Sciences, Macquarie University.

ORCID

R. L. Gardner http://orcid.org/0000-0001-8707-8537
N. R. Daczko http://orcid.org/0000-0002-3737-3818
S. Piazolo http://orcid.org/0000-0001-7723-8170

Data availability statement

Mineral chemistry EMP data are available in figshare at https://doi.org/10.6084/m9.figshare.24123258

References

Agar, S., & Lloyd, G. E. (1997). 7. Deformation of Fe–Ti oxides in gabbrois shear zones from the MARK area. In J. A. Karson, M. Cannat, D. J. Miller, & D. Elthon (Eds.), *Proceedings of the Ocean Drilling Program, Scientific Results* (Vol. 153, pp. 123–141). Ocean Drilling Program. https://doi.org/10.2973/odp.proc.sr.153.009.1997

Agar, S. M., Casey, J. F., & Kempton, P. D. (1997). 6. Textural, geochemical, and isotropic variations in gabbroic shear zones from the MARK area. In J. A. Karson, M. Cannat, D. J. Miller, & D. Elthon (Eds.), *Proceedings of the Ocean Drilling Program, Scientific Results* (Vol. 153, pp. 99–121). https://doi.org/10.2973/odp.proc.sr.153.007.1997

Basch, V., Sanfilippo, A., Skolotnev, S., Ferrando, C., Muccini, F., Palmiotto, C., Peyve, A., Ermolaev, B. V., Okina, O., & Ligi, M. (2022). Genesis of oceanic oxide gabbros and gabbronorites during reactive melt migration at transform walls (Doldrums Megatransform System; 7–8 N Mid-Atlantic Ridge). *Journal of Petrology*, *63*(9), egac086. https://doi.org/10.1093/petrology/egac086

Blackman, D. K. (2006). Site U1309. In D. K. Blackman, B. Ildefonse, B. John, Y. Ohara, D. J. Miller, C. J. MacLeod, & Expedition Scientists (Eds.), *Proceedings of the Integrated Ocean Drilling Program. Integrated Ocean Drilling Program*. https://doi.org/10.2204/iodp.proc.304305.103.2006

Blackman, D. K., Ildefonse, B., John, B., Ohara, Y., Miller, D. J., MacLeod, C. J., & Expedition 304/305 Scientists. (2006a). *Proceedings of the Integrated Ocean Drilling Program*, 304/305. Integrated Ocean Drillling Program. https://doi.org/10.2204/iodp.proc.304305.2006

Blackman, D. K., Ildefonse, B., John, B., Ohara, Y., Miller, D. J., MacLeod, C. J., & Expedition 304/305 Scientists. (2006b). *Proceedings of the IODP, 304/305*. Integrated Ocean Drilling Program. https://publications.iodp.org/proceedings/304_305/30405toc.htm

Boulanger, M., France, L., Deans, J., Ferrando, C., Lissenberg, J., & von der Handt, A. (2020). Magma reservoir formation and evolution at a slow-spreading center (Atlantis Bank, Southwest Indian Ridge). *Frontiers in Earth Science*, *8*, 554598, 24 p. https://doi.org/10.3389/feart.2020.554598

Brun, J-P., Sokoutis, D., Tirel, C., Gueydan, F., Van Den Driessche, J., & Beslier, M-O. (2018). Crustal versus mantle core complexes. *Tectonophysics*, *746*, 22–45. https://doi.org/10.1016/j.tecto.2017.09.017

Buck, W. R., Lavier, L. L., & Poliakov, A. N. B. (2005). Modes of faulting at mid-ocean ridges. *Nature*, *434*(7034), 719–723. https://doi.org/10.1038/nature03358

Cannat, M., Ceuleneer, G., & Fletcher, J. (1997). 5. Localization of ductile strain and the magmatic evolution of baggroic rocks drilled a the Mid-Altantic Ridge (23°N). In J. A. Karson, M. Cannat, D. J. Miller, & D. Elthon (Eds.), *Proceedings of the Ocean Drilling Program, Scientific Results.* Ocean Drilling Program (Vol. 153, pp. 77–98). https://doi.org/10.2973/odp.proc.sr.153.006.1997

Cannat, M., Karson, J. A., Miller, D. J., Agar, S. M., Barling, J., Casey, J. F., Ceuleneer, G., Dilek, Y., Fletcher, J., Fujibayashi, N., Gaggero, L., Gee, J. S., Hurst, S. D., Kelley, D. S., Kempton, P. D., Lawrence, R. M., Marchig, V., Mutter, C., Niida, K., Rodway, K., … Miller, D. J. (1995). *Proceedings of the ODP, Initial reports 153*. Ocean Drilling Program. https://www-odp.tamu.edu/publications/153_IR/153TOC.HTM

Casini, L., Maino, M., Sanfilippo, A., Ildefonse, B., & Dick, H. J. B. (2021). High-temperature strain localization and the nucleation of oceanic core complexes (16.5°N, Mid-Atlantic Ridge). *Journal of Geophysical Research: Solid Earth*, *126*(9), e2021JB022215. https://doi.org/10.1029/2021JB022215

Coogan, L., Jenkin, G., & Wilson, R. (2007). Contrasting cooling rates in the lower oceanic crust at fast-and slow-spreading ridges revealed by geospeedometry. *Journal of Petrology*, *48*(11), 2211–2231. https://doi.org/10.1093/petrology/egm057

Daczko, N. R., & Piazolo, S. (2022). Recognition of melferite–A rock formed in syn-deformational high-strain melt-transfer zones through sub-solidus rocks: A review and synthesis of microstructural criteria. *Lithos*, *430-431*, 106850. https://doi.org/10.1016/j.lithos.2022.106850

Daczko, N. R., Piazolo, S., Meek, U., Stuart, C. A., & Elliott, V. (2016). Hornblendite delineates zones of mass transfer through the lower crust. *Scientific Reports*, *6*(1), 31369. https://doi.org/10.1038/srep31369

Deans, J. R. L., & Yoshinobu, A. S. (2019). Geographically re-oriented magmatic and metamorphic foliations from ODP Hole 735B Atlantis Bank, Southwest Indian Ridge: Magmatic intrusion and crystal-plastic overprint in the footwall of an oceanic core complex. *Journal of Structural Geology*, *126*, 1–10. https://doi.org/10.1016/j.jsg.2019.05.001

Dick, H. J. B., Kvassnes, A. J. S., Robinson, P. T., MacLeod, C. J., & Kinoshita, H. (2019). The Atlantis Bank Gabbro Massif, Southwest Indian Ridge. *Progress in Earth and Planetary Science*, *6*(1), 64. https://doi.org/10.1186/s40645-019-0307-9

Dick, H. J. B., Natland, J. H., Miller, D. J., Alt, J. C., Bach, W., Bideau, D., Gee, J. S., Haggas, S., Hertogen, J. G. H., Hirth, G., Holm, P. M., Ildefonse, B., Iturrino, G. J., John, B., Kelley, D. S., Kikawa, E., Kingdon, A., Le Roux, P., Maeda, J., … Yoshinobu, A. (1999a). 1. Leg 176 Summary. In J. A. Marin & J. M. Scroggs (Eds.), *Proceedings of the International Ocean Drilling Program, Initial Reports* (Vol. 176, pp. 1–70). https://doi.org/10.2973/odp.proc.ir.176.1999

Dick, H. J. B., Natland, J. H., Miller, D. J., Alt, J. C., Bach, W., Bideau, D., Gee, J. S., Haggas, S., Hertogen, J. G. H., Hirth, G., Holm, P. M., Ildefonse, B., Iturrino, G. J., John, B., Kelley, D. S., Kikawa, E., Kingdon, A., Le Roux, P., Maeda, J., … Yoshinobu, A. (1999b). 3. Site 735. In J. A. Marin & J. M. Scroggs (Eds.), *Proceedings of the International Ocean Drilling Program, Initial Reports* (Vol. 176, pp. 1–313). https://doi.org/10.2973/odp.proc.ir.176.103.1999

Dick, H. J. B., Ozawa, K., Meyer, P. S., Niu, Y., Robinson, P. T., Constantin, M., Hebert, R., Maeda, J., Natland, J. H., Hirth, J. G., Mackie, S. M. (2002). 10. Primary silicate mineral chemistry of a 1.5-km section of very slow spreading lower ocean crust: ODP hole 735B, Southwest Indian Ridge. In J. H. Natland, H. J. B. Dick, D. J. Miller, & R. P. Von Herzen (Eds.), *Proceedings of the Ocean Drilling Program, Scientific Results* (Vol. 176, pp. 1–61). https://doi.org/10.2973/odp.proc.sr.176.001.2002

Dick, H. J. B., Tivey, M. A., & Tucholke, B. E. (2008). Plutonic foundation of a slow-spreading ridge segment: Oceanic core complex at Kane Megamullion, 23°30′N, 45°20′W. *Geochemistry, Geophysics, Geosystems*, *9*(5), Q05014, 44 p. https://doi.org/10.1029/2007GC001645

Drouin, M., Ildefonse, B., & Godard, M. (2010). A microstructural imprint of melt impregnation in slow spreading lithosphere: Olivine-rich troctolites from the Atlantis Massif, Mid-Atlantic Ridge, 30 N, IODP Hole U1309D. *Geochemistry, Geophysics, Geosystems*, *11*(6), Q06003, 21 p. https://doi.org/10.1029/2009GC002995

Ferrando, C., Godard, M., Ildefonse, B., & Rampone, E. (2018). Melt transport and mantle assimilation at Atlantis Massif (IODP Site U1309): Constraints from geochemical modeling. *Lithos*, *323*, 24–43. https://doi.org/10.1016/j.lithos.2018.01.012

Frassi, C., Musumeci, G., Zucali, M., Mazzarini, F., Rebay, G., & Langone, A. (2017). The Cotoncello Shear Zone (Elba Island, Italy): The deep root of a fossil oceanic detachment fault in the Ligurian ophiolites. *Lithos*, *278-281*, 445–463. https://doi.org/10.1016/j.lithos.2017.02.015

Fusseis, F., Regenauer-Lieb, K., Liu, J., Hough, R. M., & De Carlo, F. (2009). Creep cavitation can establish a dynamic granular fluid pump in ductile shear zones. *Nature*, *459*(7249), 974–977. https://doi.org/10.1038/nature08051

Gao, Y., Hoefs, J., Hellebrand, E., von der Handt, A., & Snow, J. E. (2007). Trace element zoning in pyroxenes from ODP Hole 735B gabbros: Diffusive exchange or synkinematic crystal fractionation? *Contributions to Mineralogy and Petrology*, *153*(4), 429–442. https://doi.org/10.1007/s00410-006-0158-4

Gardner, R., Piazolo, S., Daczko, N. R., & Evans, L. (2019). Ductile deformation without localization: Insights from numerical modelling. *Geochemistry, Geophysics, Geosystems*, *20*(12), 5710–5726. https://doi.org/10.1029/2019GC008633

Gardner, R. L., Piazolo, S., Daczko, N. R., & Trimby, P. (2020). Microstructures reveal multistage melt present strain localisation in mid-ocean gabbros. *Lithos*, *366-367*, 105572. https://doi.org/10.1016/j.lithos.2020.105572

Ghatak, H., Gardner, R. L., Daczko, N. R., Piazolo, S., & Milan, L. (2022). Oxide enrichment by syntectonic melt–rock interaction. *Lithos*, *414-415*, 106617. https://doi.org/10.1016/j.lithos.2022.106617

Harigane, Y., Michibayashi, K., & Ohara, Y. (2008). Shearing within lower crust during progressive retrogression: Structural analysis of gabbroic rocks from the Godzilla Mullion, an oceanic core complex in the Parece Vela backarc basin. *Tectonophysics*, *457*(3-4), 183–196. https://doi.org/10.1016/j.tecto.2008.06.009

Hirth, G., & Kohlstedt, D. L. (1995). Experimental constraints on the dynamics of the partially molten upper mantle: Deformation in the diffusion creep regime. *Journal of Geophysical Research: Solid Earth*, *100*(B2), 1981–2001. https://doi.org/10.1029/94JB02128

Holtzman, B., Kohlstedt, D. L., Zimmerman, M. E., Heidelbach, F., Hiraga, K., & Hustoft, J. (2003). Melt segregation and strain partitioning: Implications for seismic anisotropy and mantle flow. *Science*, *301*(5637), 1227–1230. https://doi.org/10.1126/science.1087132

Holyoke, C. W., III, & Tullis, J. (2006). The interaction between reaction and deformation: An experimental study using a biotite + -plagioclase + quartz gneiss. *Journal of Metamorphic Geology*, *24*(8), 743–762. https://doi.org/10.1111/j.1525-1314.2006.00666.x

Howell, S. M., Olive, J-A., Ito, G., Behn, M. D., Escartín, J., & Kaus, B. (2019). Seafloor expression of oceanic detachment faulting reflects gradients in mid-ocean ridge magma supply. *Earth and Planetary Science Letters*, *516*, 176–189. https://doi.org/10.1016/j.epsl.2019.04.001

Ildefonse, B., Blackman, D. K., John, B., Ohara, Y., Miller, D. J., MacLeod, C. J., & the IODP Expeditions 304–305 Scientists. (2006). IODP Expeditions 304 & 395 characterize the lithology, structure, and alteration of an oceanic core complex. *Science Drilling*, *3*(4), 11. https://doi.org/10.2204/iodp.sd.3.01.2006

Ildefonse, B., Blackman, D. K., John, B. E., Ohara, Y., Miller, D. J., MacLeod, C. J., & Integrated Ocean Drilling Program Expeditions 304/305 Science Party. (2007). Oceanic core complexes and crustal accretion at slow-spreading ridges. *Geology*, *35*(7), 623–626. https://doi.org/10.1130/G23531A.1

Ligi, M., Cuffaro, M., Muccini, F., & Bonatti, E. (2022). Generation and evolution of the oceanic lithosphere in the North Atlantic. *La Rivista del Nuovo Cimento*, *45*(9), 587–659. https://doi.org/10.1007/s40766-022-00035-0

Linckens, J., Herwegh, M., & Müntener, O. (2015). Small quantity but large effect—How minor phases control strain localization in upper mantle shear zones. *Tectonophysics*, *643*, 26–43. https://doi.org/10.1016/j.tecto.2014.12.008

Lissenberg, C. J., & MacLeod, C. J. (2016). A reactive porous flow control on mid-ocean ridge magmatic evolution. *Journal of Petrology*, *57*(11-12), 2195–2220. https://doi.org/10.1093/petrology/egw074

MacLeod, C. J., Carlut, J., Escartín, J., Horen, H., & Morris, A. (2011). Quantitative constraint on footwall rotations at the 15° 45′N oceanic core complex, Mid-Atlantic Ridge: Implications for oceanic detachment fault processes. *Geochemistry, Geophysics, Geosystems*, *12*(5), Q0AG03, 29 p. https://doi.org/10.1029/2011GC003503

MacLeod, C. J., Dick, H. J. B., Blum, P., Abe, N., Blackman, D. K., Bowles, J. A., Cheadle, M. J., Cho, K., Ciazela, J., Deans, J. R., Edgcomb, V. P., Ferrando, C., France, L., Ghosh, B., Ildefonse, B., Kendrick, M. A., Koepke, J., Leong, J. A. M., Liu, C., … Viegas, G. (2017). Site U1473. In C. J. MacLeod, H. J. B. Dick, P. Blum, & Expedition Scientists (Eds.), *Southwest Indian Ridge lower crust and moho. Proceedings of the International Ocean Discovery Program, 360* (pp. 1–136). International Ocean Discovery Program. https://doi.org/10.14379/iodp.proc.360.103.2017

MacLeod, C. J., Searle, R., Murton, B., Casey, J., Mallows, C., Unsworth, S., Achenbach, K., & Harris, M. (2009). Life cycle of oceanic core complexes. *Earth and Planetary Science Letters*, *287*(3-4), 333–344. https://doi.org/10.1016/j.epsl.2009.08.016

Meek, U., Piazolo, S., & Daczko, N. R. (2019). The field and microstructural signatures of deformation-assisted melt transfer: Insights from magmatic arc lower crust, New Zealand. *Journal of Metamorphic Geology*, *37*(6), 795–821. https://doi.org/10.1111/jmg.12488

Mehl, L., & Hirth, G. (2008). Plagioclase preferred orientation in layered mylonites: Evaluation of flow laws for the lower crust. *Journal of Geophysical Research*, *113*(B5), B05202, 19 p. https://doi.org/10.1029/2007JB005075

Miranda, E. A., & John, B. E. (2010). Strain localization along the Atlantis Bank oceanic detachment fault system, Southwest Indian Ridge. *Geochemistry, Geophysics, Geosystems*, *11*(4), Q04002, 33 p. https://doi.org/10.1029/2009GC002646

Nguyen, D., Morishita, T., Soda, Y., Tamura, A., Ghosh, B., Harigane, Y., France, L., Liu, C., Natland, J., Sanfilippo, A., MacLeod, C., Blum, P., & Dick, H. (2018). Occurrence of felsic rocks in oceanic gabbros from IODP hole U1473A: Implications for evolved melt migration in the lower oceanic crust. *Minerals*, *8*(12), 583. https://doi.org/10.3390/min8120583

Silva, D., Daczko, N. R., Piazolo, S., & Raimondo, T. (2022). Glimmerite: A product of melt–rock interaction within a crustal-scale high-strain zone. *Gondwana Research*, *105*, 160–184. https://doi.org/10.1016/j.gr.2021.09.005

Stuart, C. A., Piazolo, S., & Daczko, N. R. (2016). Mass transfer in the lower crust: Evidence for incipient melt assisted flow along grain boundaries in the deep arc granulites of Fiordland, New Zealand. *Geochemistry, Geophysics, Geosystems*, *17*(9), 3733–3753. https://doi.org/10.1002/2015GC006236

Stuart, C. A., Piazolo, S., & Daczko, N. R. (2018). The recognition of former melt flux through high-strain zones. *Journal of Metamorphic Geology*, *36*(8), 1049–1069. https://doi.org/10.1111/jmg.12427

Taufner, R., Viegas, G., Faleiros, F. M., Castellan, P., & Silva, R. (2021). Deformation mechanisms of granulite-facies mafic shear zones from hole U1473A, Atlantis Bank, Southwest Indian Ridge (IODP Expedition 360). *Journal of Structural Geology*, *149*, 104380. https://doi.org/10.1016/j.jsg.2021.104380

Vernon, R. (2011). Microstructures of melt-bearing regional metamorphic rocks. In D. D. van Reenen, J. D. Kramers, S. McCourt, & L. L. Perchuk (Eds.), *Origin and Evolution of Precambrian High-Grade Gneiss Terranes, with Special Emphasis on the Limpopo Complex of Southern Africa*. Geological Society of America Memoirs (Vol. 207, pp. 11.). https://doi.org/10.1130/2011.1207(01)

Whattam, S. A., Früh-Green, G. L., Cannat, M., De Hoog, J. C. M., Schwarzenbach, E. M., Escartin, J., John, B. E., Leybourne, M. I., Williams, M. J., Rouméjon, S., Akizawa, N., Boschi, C., Harris, M., Wenzel, K., McCaig, A., Weis, D., & Bilenker, L. (2022). Geochemistry of serpentinized and multiphase altered Atlantis Massif peridotites (IODP Expedition 357): Petrogenesis and discrimination of melt–rock vs. fluid-rock processes. *Chemical Geology*, *594*, 120681. https://doi.org/10.1016/j.chemgeo.2021.120681

Whitney, D. L., & Evans, B. W. (2010). Abbreviations for names of rock-forming minerals. *American Mineralogist*, *95*(1), 185–187. https://doi.org/10.2138/am.2010.3371

Whitney, D. L., Teyssier, C., Rey, P., & Buck, W. R. (2013). Continental and oceanic core complexes. *Geological Society of America Bulletin*, *125*(3-4), 273–298. https://doi.org/10.1130/B30754.1

Wijns, C., Weinberg, R., Gessner, K., & Moresi, L. (2005). Mode of crustal extension determined by rheological layering. *Earth and Planetary Science Letters*, *236*(1-2), 120–134. https://doi.org/10.1016/j.epsl.2005.05.030

Wolff, P. E., Koepke, J., & Feig, S. T. (2013). The reaction mechanism of fluid-induced partial melting of gabbro in the oceanic crust. *European Journal of Mineralogy*, *25*(3), 279–298. https://doi.org/10.1127/0935-1221/2013/0025-2314

Zhang, W-Q., Dick, H. J. B., Liu, C-Z., Lin, Y-Z., & Angeloni, L. M. (2021). MORB melt transport through Atlantis Bank Oceanic Batholith (SW Indian Ridge). *Journal of Petrology*, *62*(6), egab034, 35 p. https://doi.org/10.1093/petrology/egab034

Zhang, W-Q., Liu, C-Z., & Dick, H. J. B. (2020). Evidence for multi-stage melt transport in the lower ocean crust: The Atlantis Bank Gabbroic Massif (IODP Hole U1473A, SW Indian Ridge). *Journal of Petrology*, *61*(9), egaa082, 33 p. https://doi.org/10.1093/petrology/egaa082